J Intell Robot Syst (2015) 80:139–164
DOI 10.1007/s10846-014-0145-3

Development and Modeling of a Low-Cost Unmanned Aerial Vehicle Research Platform

Ony Arifianto · Mazen Farhood

Received: 3 February 2014 / Accepted: 1 October 2014 / Published online: 31 October 2014

Abstract This paper describes the development and modeling of a low-cost and reliable small unmanned aerial vehicle research platform for advanced control implementation. The platform is mostly constructed of low-cost commercial-off-the-shelf (COTS) components. The only non-COTS components are the airdata probes, which are manufactured and calibrated in-house. The airframe used is the commercially available radio-controlled (R/C) 6-foot Telemaster airplane from Hobby Express, chosen mainly for its adequately spacious fuselage and for being reasonably stable and sufficiently agile. One noteworthy feature of this platform is the use of two separate low-cost onboard computers for handling the data management/hardware interfacing and control computation. Specifically, the single board computer, Gumstix Overo Fire, is used to execute the control algorithms, whereas the open source autopilot, Ardupilot Mega, is mostly used to interface the Overo computer with the sensors and actuators. The platform supports multi-vehicle operations through the use of a radio modem that enables multi-point communications. As the goal of this platform is to implement rigorous control algorithms for real-time trajectory tracking and distributed control, it is important to derive an appropriate flight dynamic model of the platform, based on which the controllers will be synthesized. For that matter, the paper provides reasonably accurate models of the vehicle, servomotors, and propulsion system. Namely, the output error method is used to estimate the longitudinal and lateral-directional aerodynamic parameters from flight test data. The moments of inertia of the platform are determined using the simple pendulum test method, and the frequency response of each servomotor is also obtained experimentally. The Javaprop applet is used to obtain lookup tables relating airspeed to propeller thrust at constant throttle settings.

Keywords Unmanned aerial vehicle · Small fixed-wing aircraft · Five-hole probe · Flight dynamic model · Time-domain system identification

1 Introduction

The many appealing features of unmanned aerial vehicles (UAVs), such as persistence and versatility, have rendered these systems very useful for a wide range of military, civilian, and research applications, including real-time reconnaissance, surveillance, and target acquisition, atmospheric sciences, and disaster relief. The focus of this paper is miniature-sized (less than 2 meter wing span), low-cost, but highly capable fixed-wing UAVs. Such UAVs can be deployed in groups to perform complex and intricate tasks, and hence

O. Arifianto · M. Farhood (✉)
Department of Aerospace and Ocean Engineering, Virginia Tech, Blacksburg, VA 24061, USA
e-mail: farhood@vt.edu

O. Arifianto
e-mail: oarifianto@vt.edu

can serve as a viable alternative to dispatching larger expensive high-tech aerial vehicles in certain applications. The appealing low-cost feature, which makes these UAVs expendable, is due partly to the use of relatively cheap sensors, actuators, and processors. In addition, the convenient small size poses restrictions on the computational and sensing capabilities. Then, the strategy for achieving the desired high capability despite the size, weight, and cost restrictions centers around the development of new principles and novel technologies in software and hardware design.

Developing a UAV research platform to validate these new principles and technologies is of great importance, and so it is no surprise that many UAV testbeds have been developed by various academic groups, e.g., [9, 20, 25, 26, 32, 36, 38, 40, 42]. The main goal in building our testbed is to develop a low-cost and reliable fixed-wing UAV platform that can be used to implement relatively complex control algorithms. Building a low-cost UAV platform is not an original idea, as other research groups in the control and robotics community have done so. For instance, the UAV research group at the University of Minnesota have developed a low-cost UAV testbed [11, 38], which is mostly built of commercial-off-the-shelf (COTS) components and uses the radio-controlled (R/C) fixed-wing UAV, Ultra Stick 25e, as the main test aircraft. Another low-cost UAV platform, based on the R/C Goldberg Decathlon ARF airframe, has been developed at Georgia Tech [26] for educational purposes. The UAV research platform [20] uses the low-cost open source autopilot, Ardupilot Mega, and the Aero Testbed at the University of Illinois uses the Paparazzi autopilot, which is also low-cost and open source. These testbeds and others which are not mentioned here rely on COTS components as well as hardware/software developed in-house.

Our testbed also consists mostly of low-cost COTS components; the only components built in-house are the airdata probes, which are used to measure the angle of attack, sideslip, and airspeed of the UAV. The procedure for building and calibrating these sensors is based on [6, 10, 35] and discussed in sufficient details herein. The airframe used is the commercially available R/C 6-foot Telemaster Electro ARF from Hobby Express; see Fig. 1 and Table 1 for the major geometric parameters of this aircraft. This aircraft is selected primarily for its box-fuselage design, which provides ample space for onboard electronics. Furthermore, this R/C airplane is a well-known platform that is reasonably stable, yet still capable of performing certain aerobatic maneuvers. Minor modifications to the basic airframe were performed in order to place sensors both in the fuselage and on the wings. Aside from the use of standard sensors and actuators, a noteworthy feature of our platform is that the data management/hardware interfacing and control computation are performed by two separate onboard computers. Specifically, the low-cost single-board computer, Gumstix Overo Fire, is used to execute the control algorithms and ultimately compute the control commands, whereas, the COTS open source autopilot, Ardupilot Mega [1], is mostly used to interface the Gumstix computer with the sensors and actuators. The use of an

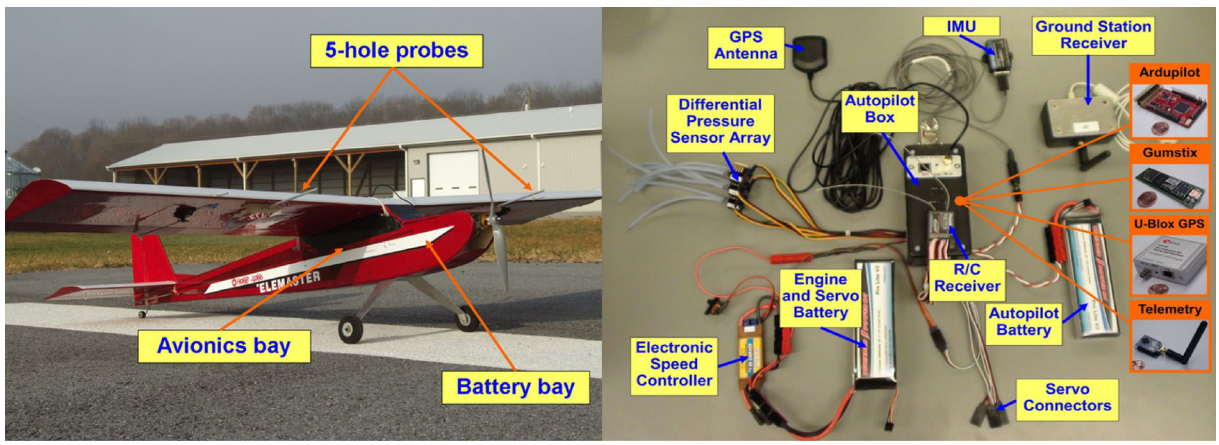

Fig. 1 A 6-foot Telemaster UAV and its onboard instruments

Table 1 Main geometrical parameters of the Telemaster

Wing area	0.56	m^2
Wing span	1.83	m
Wing MAC*	0.30	m
Mass	3.24	kg

*MAC: mean aerodynamic chord

XBee 900-Pro radio modem onboard the platform allows for data transmission among multiple vehicles, and thus the testbed also supports multi-vehicle operations.

This UAV research platform is to be used to implement systematic and rigorous approaches, developed in our research lab, on controlled maneuvers, tracking along trajectories, and distributed control, e.g., [4, 12–15], and further validate formal methods for mathematically certified control software design. As the control design methodology pursued is model based, it is important that we derive reasonably accurate models that capture the rigid-body dynamics of the vehicle and any relevant subsystems. For this application, the subsystems that directly influence the vehicle dynamics are the propulsion system and the servos that actuate the aerodynamic control surfaces. The thrust produced by the propeller is estimated using code that employs blade element theory [21]. Validation of the propulsion model is performed under static test conditions. The servomotors are modeled as single-input single-output systems based on frequency response data. The moments of inertia of the vehicle are determined experimentally by using the compound pendulum method, as described in [19, 33, 45]. A dynamic model of the aircraft is obtained via system identification. A series of flight tests are performed, and the aerodynamic parameters of the postulated model are estimated from the flight test data using the output error method (OEM), an approach that has been used widely for aircraft system identification. This approach is chosen due to its ability to handle measurement noise while maintaining a reasonable computational complexity, in contrast to the more sophisticated filter error method [24]. Since the OEM does not account for process noise, e.g., atmospheric turbulence, it is necessary that all flight tests be performed at times when minimum disturbance is observed.

A thorough review of system identification applications for various types of UAVs is given in [49]. For fixed-wing aircraft, there are several works that are similar in scope to the approach presented here. A nonlinear mapping identification algorithm is utilized in [44] in order to estimate parameters that capture the attitude dynamics of an aircraft; the parameters corresponding to the moments acting on the vehicle are formulated as a linear model using state and input variables. In [30], the output error method is utilized to estimate stability and control derivatives that capture the roll attitude dynamics from test data. Nonlinear constrained optimization is used in [26] to estimate parameters that minimize the difference between measured and model predicted output data. Both longitudinal and lateral-directional models were obtained using the linearized dynamics for each mode, respectively. In this work, the output error method will be applied in order to estimate the parameters of a model capturing the aerodynamic forces and moments for both longitudinal and lateral-directional excitations.

A number of hybrid control systems with performance guarantees (in the ℓ_2-induced norm sense) have been implemented on this UAV platform. Figure 2 shows data and snapshots from a flight test in which a hybrid feedback controller designed for the UAV executes two tasks consecutively: The first task is performing a Split-S maneuver and the second is tracking a level-turn trim condition. Due to space considerations, however, we will not be able to include in this paper a section on control design and implementation.

While the development and modeling in the sequel are focused on a specific platform, the approaches utilized are generally applicable to the entire class of small, low-cost fixed-wing UAVs. As mentioned before, the small-size and low-cost requirements for these UAVs render the use of some sophisticated measurement, instrumentation, and flight computer systems that are typically found onboard full-size aircraft infeasible, restricting as a result the computational and sensing capabilities of such UAVs. It is plausible, furthermore, that these restrictions will affect the applicability of some of the widely used system identification techniques for aircraft, and hence it is important to investigate and perhaps adjust these techniques so that they are applicable for modeling of small, low-cost aircraft. This issue has been addressed recently in [11], where a modeling method based on system identification in the frequency domain is presented. In our work, we examine a procedure for time-domain aerodynamic system identification of small, low-cost UAVs

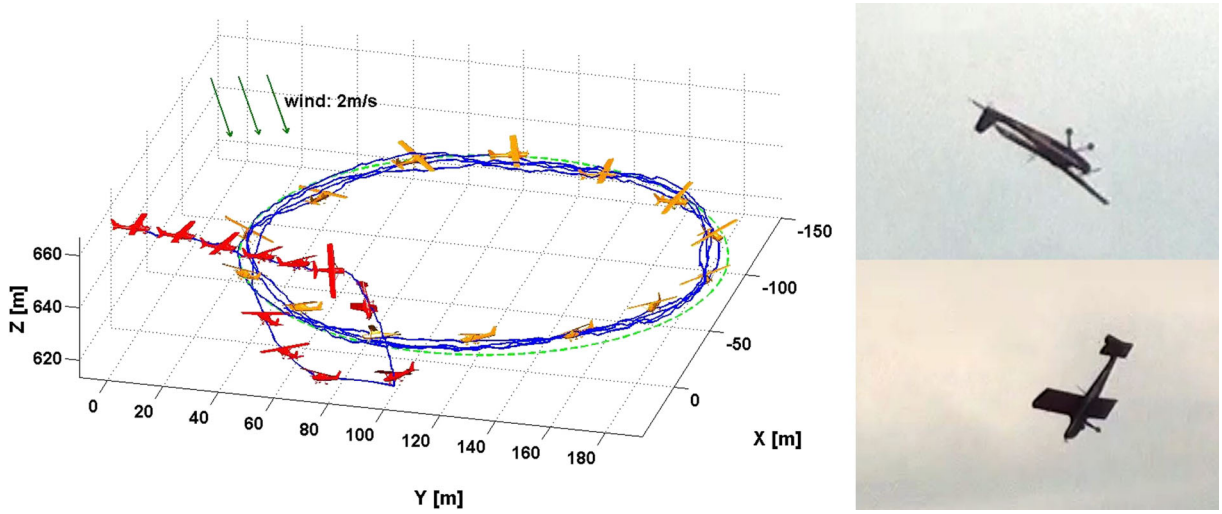

Fig. 2 The plot on the left shows the UAV executing autonomously a Split-S maneuver followed by tracking a level-turn trim condition; the pictures on the right are snapshots of the UAV as it performs the Split-S maneuver

based on the output error method, augmented for completeness with practical and easy-to-implement methods from the literature for obtaining the moments of inertia as well as the servomotor and propulsion system models. This complete modeling approach for small, low-cost UAVs is implemented on the Telemaster platform and constitutes the main contribution of this work. We also present a reliable system architecture, where two separate onboard computers are used to handle the data management/hardware interfacing and control computation, and demonstrate a cost-effective procedure for manufacturing and calibrating reasonably accurate airdata probes for small UAVs. All in all, the main outcomes of this work are as follows:

- We have developed a low-cost, small UAV research platform, which is built mostly of COTS components with a total price not exceeding $3000. The only non-COTS components are the airdata probes, which are manufactured in-house following a simple process and calibrated using the procedure from [35]. In fact, one of the goals of this paper is to show that it is inexpensive to manufacture certain types of airdata probes, which, with the proper calibration, can be reasonably accurate. Specifically, we can easily and inexpensively manufacture 5-hole probes with a conical tip shape from commercially available materials using conventional machining techniques, as discussed later in the paper. In addition, we demonstrate that an open jet tunnel is sufficient for the calibration of such probes.
- We have derived reasonably accurate models of the UAV, servos, and propulsion system. The output error method is used to estimate both the longitudinal and lateral-directional aerodynamic parameters from flight test data, which, to the authors' best knowledge, is a first for small fixed-wing UAVs.

The outline of this paper is as follows. In Section 2, we present the avionics used onboard the platform, along with the ground control station, and discuss the development of the airdata probes. In Section 3, we discuss the simple pendulum test method used to determine the moments of inertia of the vehicle, and derive the mathematical models of the UAV, servos, and propulsion system. A brief summary is provided in Section 4.

2 UAV Platform Development

This section consists of two subsections. The first describes all the components of the platform avionics and the data flow among these components. The second subsection presents the development process of

two airdata probes, which are manufactured and calibrated in-house; these sensors measure the airflow around the airplane and are used to determine the angle of attack, sideslip, and airspeed of the UAV.

2.1 System Description and Architecture

In this subsection, we discuss the electronics used onboard the platform, which consist of actuators, sensors, communication radios, and computers, as shown in Fig. 1. The online references for all the COTS components used can be found in the dissertation [3].

Actuators: The actuators are chosen based on the manufacturer's (Hobby Express) recommendations. Specifically, Futaba S3152 servos are used for aileron, elevator, and rudder control. A JETI ADVANCE 40 Pro (40 Amps programmable) electronic speed controller (ESC) is used to regulate the rotational speed of an AXI 2826/12 electric motor, which is attached to a 13x8 APC propeller.

Sensors: The sensors used include a Microstrain 3DM GX3-25 Attitude and Heading Reference System (AHRS) (to measure attitude angles, angular rates, and linear accelerations), a Ublox LEA-4T Global Positioning System (GPS) receiver (to determine position), a VTI Technologies SCP1000 static pressure sensor (to determine altitude), and two airdata probes built in-house (for airflow measurements), which use two Freescale Semiconductor MPXV7002DP differential pressure sensor arrays. Details on the development of these probes are given in Section 2.2. The following are some useful comments on the use of some of the aforementioned sensors:

- The accelerometers and rate gyros of the 3DM GX3-25 AHRS give measurements of linear accelerations and angular rates about the aircraft's body reference frame. An internal Kalman filter algorithm uses these measurements, along with those of the AHRS magnetometers, to compute the Euler attitude angles. Adjustment of the Kalman filter weights may be necessary when operating in areas with severe magnetic disturbances. In such scenarios, it is advisable to place more confidence in the measurements given by the accelerometers and rate gyros than those obtained from the magnetometers.
- The Ublox GPS receiver determines position in terms of latitude, longitude, and altitude. Ground speed and course can be computed from this data, and will be utilized in the airdata probe calibration process. In general, the precision of the altitude measurement from this automotive grade GPS is insufficient for feedback control action when tracking rapid maneuvers. To circumvent this issue, a measurement of the altitude based on pressure is used instead. The pressure altitude is determined from the static pressure measurement of the SCP1000 sensor using the standard atmospheric model [2]. To account for non-standard day conditions, a bias is introduced so that the calculated pressure altitude on the ground matches the corresponding altitude determined by the GPS.
- Since the avionics bay on the Telemaster has an opening directly behind the motor and propeller, the pressure in the compartment is directly affected by the air mass exerted by the propeller. To alleviate the resulting pressure build-up, several holes have been drilled into the fuselage. To ensure that the SCP1000 sensor and the static ports of the MPXV7002DP sensor array measure the static pressure in the fuselage, felt covers have been installed on the inlet of the sensors.

Communication radios: There are two radios onboard the platform: a Futaba R617FS eight-channel receiver used for receiving commands from the R/C transmitter and a 900MHz XBee-Pro used for transmitting data to the Ground Control Station (GCS). During multi-vehicle operations, the XBee can also be used to send and receive data among the vehicles. Specifically, this modem is capable of transmitting data to multiple modems within its range (approximately $500 - 600$ m in our setup), provided that the same identification number is shared by both the sender and the receiver. Selective sending and receiving to simulate various communication topologies is achieved through the use of a specific header for the data being sent. The header consists of the origin of the information and the target. The target can be a single vehicle, multiple vehicles, or all vehicles within communication range. An example of a communication topology is given in Fig. 3. This

figure shows 3 UAVs interconnected over a communication network in a follow-the-leader type experiment, where the UAV in the red rectangle is the leader and the other two UAVs are the followers. The leader sends data to the ground station and to both follower UAVs, and receives commands from the ground station. The follower UAVs send data to each other and to the ground station.

Computers: The platform uses two low-cost, open source computers: Ardupilot Mega and Gumstix Overo Fire. Ardupilot is used solely for data management/hardware interfacing, which boils down to reading data from sensors, transmitting data to actuators and other instruments, and recording data for later analysis. This open source autopilot hardware has full autopilot capabilities. Its accompanying software is fully accessible and thus can be significantly altered, or, if necessary, rewritten. Ardupilot has different types of serial ports (I2C, SPI, and 4 UART) that can be used to connect to a variety of sensors. It has 16 analog-to-digital converters to handle sensors with analog voltage outputs as well as 8 pulse-width modulation (PWM) input channels and 8 PWM output channels that can be used to drive servos. These features, along with the flexibility of the firmware, render the board adaptable to a variety of sensor configurations.

All control computations are carried out by the Gumstix Overo Fire computer, which is a single board computer powered by a 600MHz OMAP3530 microprocessor from Texas Instruments. The Overo runs a Linux Angstrom distribution as its operating system, and the control algorithms are implemented in the Python programming language. This computer is primarily selected for its small size. With length, width, and height dimensions of 58 mm, 17 mm, and 4.2 mm, respectively, the Overo is advantageous for small UAV applications where space and mass are major constraints. The Overo exchanges data with Ardupilot via a serial port.

Before concluding this subsection, we will provide an overview of the data flow among the computers, sensors, and servos onboard the airplane. Note that the engine electronic speed controller (ESC) is considered as a servo in this scheme. A diagram of the data exchange between these components is given in Fig. 4. As the diagram shows, Ardupilot receives data from the sensors and passes this data to the Overo computer. Overo then determines the necessary control inputs based on this data and sends the calculated control commands back to Ardupilot. Based on these

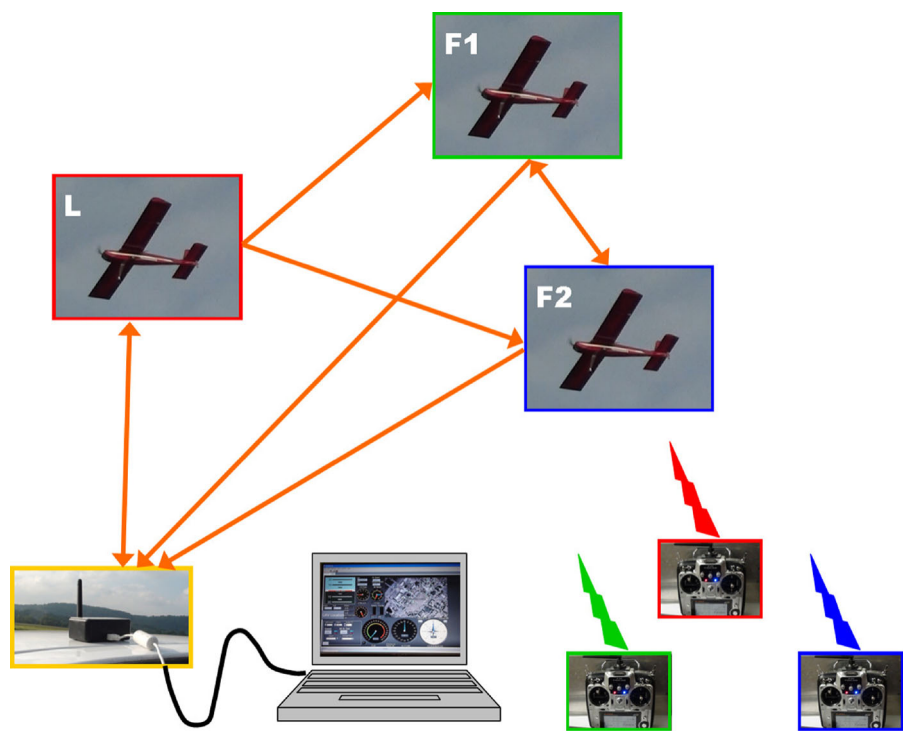

Fig. 3 3 UAVs interconnected over a communication network through the use of the Xbee radio modems

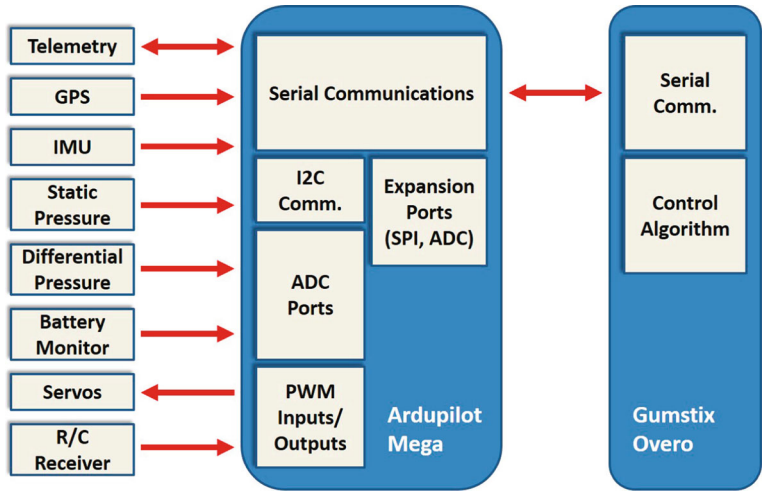

Fig. 4 A data flow diagram of the fully programmable airborne system

commands, Ardupilot actuates the servos to drive the control surfaces. Ardupilot also composes a data package, consisting of all the measurements along with the control inputs to be sent to the onboard data logger as well as the ground station through the telemetry system. On the ground, the R/C transmitter has an on/off switch, which is used to activate/deactivate the autopilot mode. Once the autopilot mode is deactivated, i.e., the UAV is operating in manual mode, the Overo computer becomes passive, while Ardupilot listens to the manual commands from the R/C transmitter and passes them through to the servos.

To completely characterize the system, analysis of the execution time for each routine in the autopilot code is performed. This is carried out by programming the autopilot to execute a particular routine for a thousand times and then recording the worst time. Worst case execution time for each task is used to make sure that all tasks can be executed within the allocated time and, further, to determine the time delay in obtaining measurements from the sensors. The worst case execution time for each task is given in Table 2.

2.2 Airdata Probe

One of the main goals of this work is deriving a reasonably accurate aerodynamic model of the UAV. As the aerodynamic forces and moments are highly dependent on the airflow velocity vector, it is essential for achieving this goal to be able to measure or, at least, estimate the angle of attack and sideslip. It is possible to estimate these angles rather accurately from the inertial velocity and attitude angles in the absence of significant winds, as demonstrated in [22] and [34]. However, the condition of no significant winds is not easily met when dealing with small UAVs flying at low speeds. Thus, developing sensors that can measure the angle of attack and sideslip is instrumental for obtaining an adequate aerodynamic model of a small UAV.

2.2.1 Probe Design and Manufacturing

Common methods for measuring the airflow direction use mechanical vanes, differential pressure tubes, or null-seeking pressure tubes, as outlined in [18]. Due to potential design and implementation difficulties, the use of mechanical vanes and null-seeking pressure tubes is not preferable in the case of small UAVs where size and weight are major constraints. To the best of our knowledge, null-seeking pressure tubes have never been used on small UAVs. Mechanical

Table 2 Worst case execution time

Task	Worst Case Execution Time [ms]
Drive servos	0.16
Read static pressure	0.96
Read IMU (AHRS)	1.69
Read airdata	1.77
Ardupilot-Gumstix data exchange	8.4
Send data to ground	12.55

vanes, on the other hand, have been used successfully on a small UAV in [40] to measure the airflow direction.

There are various differential probe designs that can be used to measure the airflow vector. These designs vary in the shape of the probe tip and/or the number of pressure holes. A comparison of measurement results using different designs of differential probes is given in [6]. As stated in [46], the accuracy of the differential probe measurements is proportional to the number of pressure holes, and hence comes at the expense of increased manufacturing complexity. The shape of the tip also affects the accuracy of the probe measurements. For instance, an airdata probe with a perfectly spherical tip shape gives accurate measurements without the need for calibration because there are mathematical formulas available in the literature that can be used to directly compute the airspeed, angle of attack, and sideslip from the pressure differences in this case. Manufacturing such a probe, however, is challenging. In our case, we have opted to design a five-hole probe with a conical tip shape for the following reasons: (1) There are many publications on the calibration and testing of five-hole probes; and (2) it is possible to manufacture this probe from commercially available materials using conventional machining techniques. We have built and calibrated two probes, each mounted on a wing of the airplane at a distance of 406.4 mm (16 inches) from the plane of symmetry with the port holes situated about 152.4 mm (6 inches) from the wing leading edge; see Fig. 1. This configuration maintains lateral balance and ensures that the effects of the propeller wash and wing interference on the airflow measurements are insignificant. Both probes are comparable in quality and are used together in our platform for redundancy. In the following, we will just focus on one probe.

The CAD model of the five-hole probe that we have designed is given in Fig. 5, along with the final product. The figure shows the holes arrangement at the tip of the probe. The probe consists of five small aluminum tubes, glued together using JB Weld plastic steel to form the desired plus-sign configuration, and then encased in a larger aluminum tube. The tubes used are sold in most hardware stores. The length of the probe is 203.2 mm, and the tip diameter is 5.56 mm. Each of the five small tubes has an outer diameter of 1.60 mm and an inner diameter (hole diameter) of 0.89 mm. Then, the ratio of the hole diameter to the tip diameter is 0.16. Although this ratio is relatively small compared to the one in [6], the number is fairly close to newer designs, such as those in [39] and [41].

The tip design is conical with 90° angle. As observed in [6, 10], this tip design yields reasonably accurate measurements of the angle of attack and sideslip at low speeds and can be calibrated to measure these angles within the range ±22.5°. For such a tip design, there are no mathematical formulas that directly relate the pressure differences to the angle of attack and sideslip, as in the case of the perfectly spherical tip shape. Hence, the relationship between the measured pressure at each hole (port) and the airflow velocity vector can only be determined by experiment. The experiment, along with the required data processing and curve fitting, is henceforth referred to as probe calibration.

2.2.2 Probe Calibration

The calibration of the probe was performed in the Subsonic Open Jet Wind Tunnel at Virginia Tech following the procedure given in [35]. Figure 6 shows the experiment setup. In this setup, the probe is placed in the middle of the test section of the wind tunnel on a turntable that can be rotated to vary the sideslip angle. The angle of attack can also be varied by rotating the rod on which the turntable is mounted. During calibration, the rotational speed of the wind tunnel fan is increased from 0 to 1180 rpm (maximum achievable

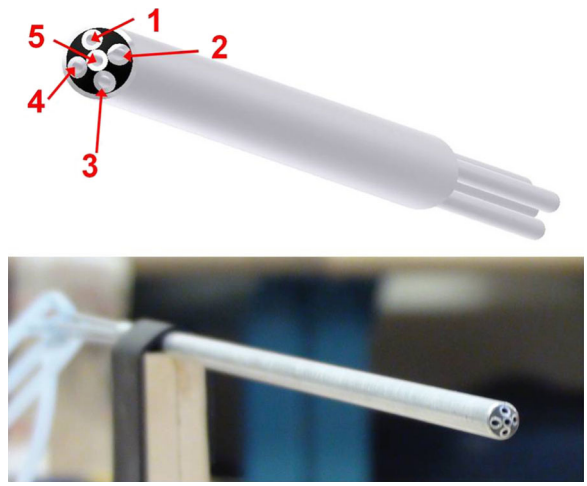

Fig. 5 Five-hole probe and its CAD drawing

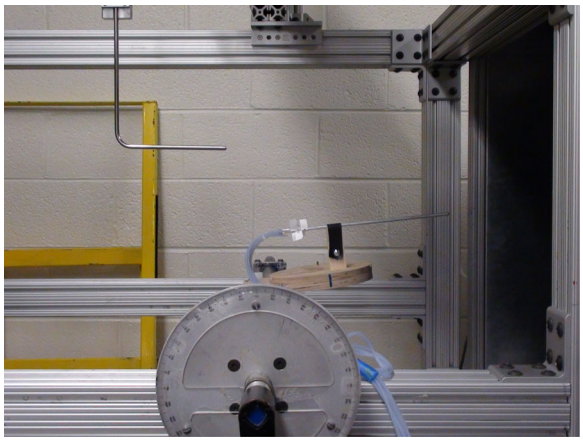

Fig. 6 Five-hole probe calibration process

speed) in increments of 200 rpm. The airflow velocity (in m/s) is about 0.021 times the fan rotational speed (in rpm). Hence, at a fan speed of 1180 rpm, the resultant airflow velocity is about 24.78 m/s. For each considered rotational speed, the angle of attack and sideslip are varied from $-20°$ to $+20°$ in $5°$ increments, with the pressure at all ports of the probe measured in each configuration. The pressure measurements for various values of the angle of attack and sideslip at a fan speed of 400 rpm are shown in Fig. 7.

As aforementioned, during calibration, the pressures at all ports of the probe, i.e., $p_1, p_2, \ldots, p_5$, are measured for each configuration, where p_i is the pressure at port i and the port numbering is shown in Fig. 5. As given in [35], it is possible to approximately compute the angle of attack, α, and sideslip, β, from the pressures $p_1, \ldots, p_5$ as follows:

$$\alpha = \frac{a_0+a_1C_{p_\alpha}+a_2C_{p_\beta}+a_3C_{p_\beta}^2+a_4C_{p_\beta}^3}{1+a_5C_{p_\alpha}+a_6C_{p_\beta}+a_7C_{p_\beta}^2+a_8C_{p_\beta}^3}, \quad (1)$$

$$\beta = \frac{b_0+b_1C_{p_\alpha}+b_2C_{p_\beta}+b_3C_{p_\alpha}^2+b_4C_{p_\beta}^2+b_5C_{p_\alpha}C_{p_\beta}}{1+b_6C_{p_\alpha}+b_7C_{p_\beta}+b_8C_{p_\alpha}^2+b_9C_{p_\beta}^2+b_{10}C_{p_\alpha}C_{p_\beta}}, \quad (2)$$

where $p_{av} = 0.25(p_1 + p_2 + p_3 + p_4)$, $C_{p_\alpha} = \frac{p_3-p_1}{p_5-p_{av}}$, and $C_{p_\beta} = \frac{p_4-p_2}{p_5-p_{av}}$. Given the data collected in the calibration process, the coefficients $a_0, a_1, \ldots, a_8$ and $b_0, b_1, \ldots, b_{10}$ in equations (1–2) are obtained by solving a least-squares problem by linear regression. The fitting surface and goodness of fit for the angle of attack and sideslip are shown in Fig. 8. The coefficient of determination, or R^2, value for the angle of attack data fitting is 0.9949 and that for the sideslip data fitting is 0.9972.

The airspeed V_a can be computed from the static pressure p_s and total pressure p_t, namely,

$$V_a = \sqrt{\frac{2(p_t - p_s)}{\rho}},$$

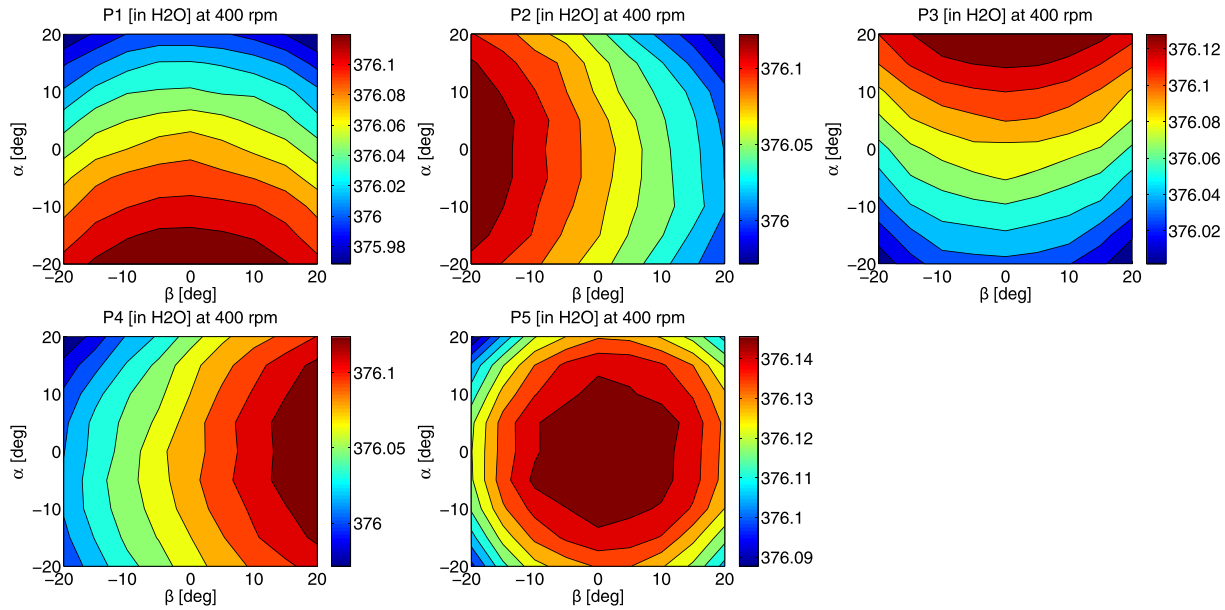

Fig. 7 Pressure distribution at various values of the angle of attack (α) and sideslip (β) for all ports of the probe

where ρ denotes the air density. While it is possible to measure p_s and p_t during calibration by using a pitot-static tube aligned with the direction of the airflow, it is impractical to replicate this setup on the actual UAV. Alternatively, as suggested in [35], we can approximately obtain the values of the static and total pressures, and hence the airspeed, from the angle of attack and sideslip, along with the pressures $p_1, \ldots, p_5$, as follows:

$$p_s = \frac{C_{p_5} p_{av} - C_{pav} p_5}{C_{p_5} - C_{pav}} \text{ and } p_t = p_s + \frac{p_5 - p_s}{C_{p_5}},$$

where

$$C_{p_5} = \frac{c_0 + c_1\beta + c_2\beta^2 + c_3\beta^3 + c_4\alpha + c_5\alpha^2}{1 + c_6\beta + c_7\alpha + c_8\alpha^2 + c_9\alpha^3} \quad (3)$$

and

$$C_{pav} = d_0 + d_1\beta + d_2\alpha + d_3\beta^2 + d_4\alpha^2 + d_5\alpha\beta + d_6\beta^3 + d_7\alpha^3 + d_8\beta\alpha^2 + d_9\beta^2\alpha. \quad (4)$$

The coefficients $c_0, c_1, \ldots, c_9$ and $d_0, d_1, \ldots, d_9$ in equations (3–4) are also obtained by solving a least-squares problem by linear regression. As shown in Fig. 9, the R^2 value for the C_{p_5} data fitting is 0.9788 and that for the C_{pav} data fitting is 0.9676. Our calibration results, and specifically the R^2 values, are comparable to those obtained in [35]. This observation is noteworthy considering that the authors in [35] utilize a more sophisticated manufacturing process in building their probe, in addition to a closed-circuit wind tunnel for calibration, which generally generates less turbulent airflow compared to an open-jet tunnel.

2.2.3 Validation and Analysis

The calibration results are validated by wind-tunnel testing as well as flight testing. In the wind-tunnel tests, the probe is evaluated at a low airflow speed of about 12 m/s and a high airflow speed of about 20 m/s; these speeds correspond to the lower and upper limits of typical operation of the UAV platform, respectively. For each speed, the angle of attack is varied from $-10°$ to $10°$ in $5°$ increments at $0°$ sideslip, and similarly, the sideslip is varied from $-10°$ to $10°$ in $5°$ increments at $0°$ angle of attack. The pressure sensors and analog-to-digital converter used in these tests are the same as those used onboard the UAV, as opposed to the high-precision pressure scanner in the wind-tunnel facility, which is used in the calibration process. In addition, a first-order low-pass filter with a cutoff frequency of 1 Hz is applied to the output of each of the pressure sensors. We choose these specific wind-tunnel validation tests as they are comparable to the flight tests carried out for aerodynamic modeling purposes.

Figure 10 shows the validation results for the considered values of the angle of attack with $0°$ sideslip at 12 m/s and 20 m/s airflow speeds. Specifically, at each speed and for each value of the angle of attack, the test is run for 30 seconds, and samples are collected at 20 Hz, i.e., we end up with 600 samples in total for each test. Thus, the total number of samples for all the angle of attack tests at each speed is 3000. The measurement error is defined as the difference between the measured value and true value of the angle of attack. We then have 3000

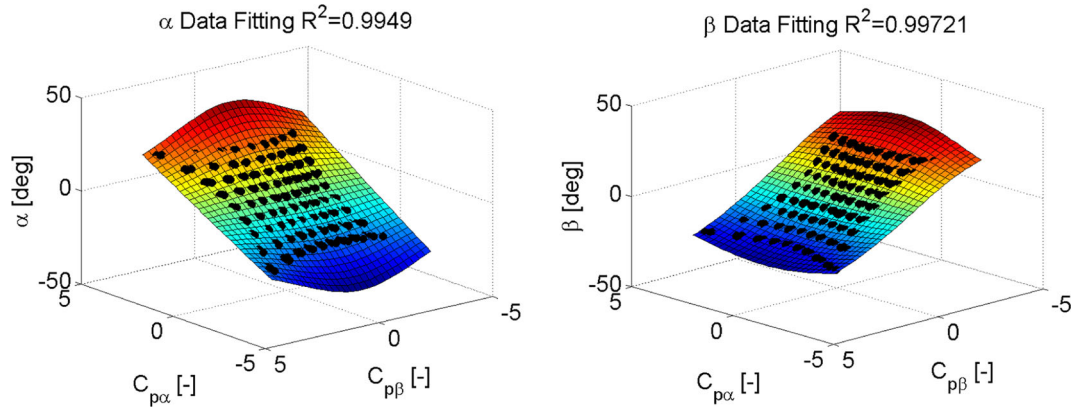

Fig. 8 Angle of attack and sideslip surface fitting

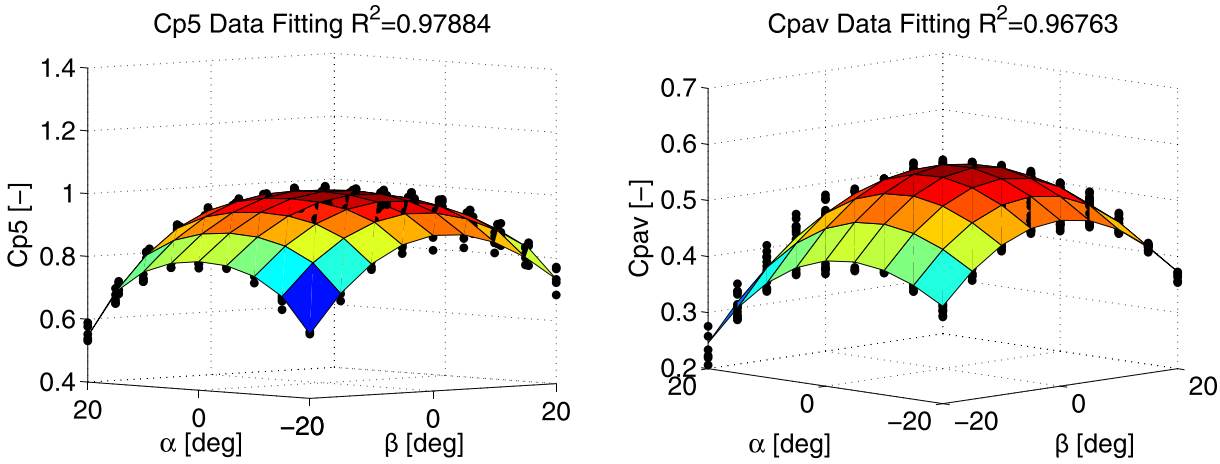

Fig. 9 C_{p_5} and $C_{p_{av}}$ surface fitting

samples of the measurement error at 12 m/s airflow speed (low speed) and another 3000 samples at 20 m/s (high speed). Note that the measurement discrepancies are due to calibration errors as well as instrumentation errors (because of the use of the actual, less accurate sensors). The following analysis of the aforementioned two sets of data is based on [50]. Given these data, we find that the angle of attack can be measured with an accuracy of 0.67° at low speed and 0.46° at high speed, where the accuracy is given in terms of the root-mean-square (RMS) of the measurement error. The RMS is defined as $\text{RMS} = \sqrt{\frac{1}{N}\sum_{i=1}^{N} e_i^2}$, where N is the number of samples, which is 3000 for each speed, and e_i is the i^{th} sample of the measurement error. The RMS measure is used because the mean of the error is not zero; specifically, there is a measurement bias of 0.27° at low speed and −0.06° at high speed. Assuming the error is normally distributed about the nonzero mean value, then, for each speed, the number of samples that lie within the range ±RMS is equal to $\frac{1}{2}\left(\text{ERF}\left(\frac{\text{RMS}-\mu}{\sigma\sqrt{2}}\right) + \text{ERF}\left(\frac{\text{RMS}+\mu}{\sigma\sqrt{2}}\right)\right)$, where σ is the standard deviation of the error, μ is the mean value, and $\text{ERF}(\eta)$ is the error function defined as $\text{ERF}(\eta) = \frac{1}{\sqrt{2}}\int_{-\eta}^{\eta} e^{-\xi^2} d\xi$. Hence, 80.6% of the measurement error samples lie within ±0.67° at low speed and 83.9% lie in the range ±0.46° at high speed. Additionally, 95% of the error samples lie in the range ±0.99° at low speed and ±0.64° at high speed.

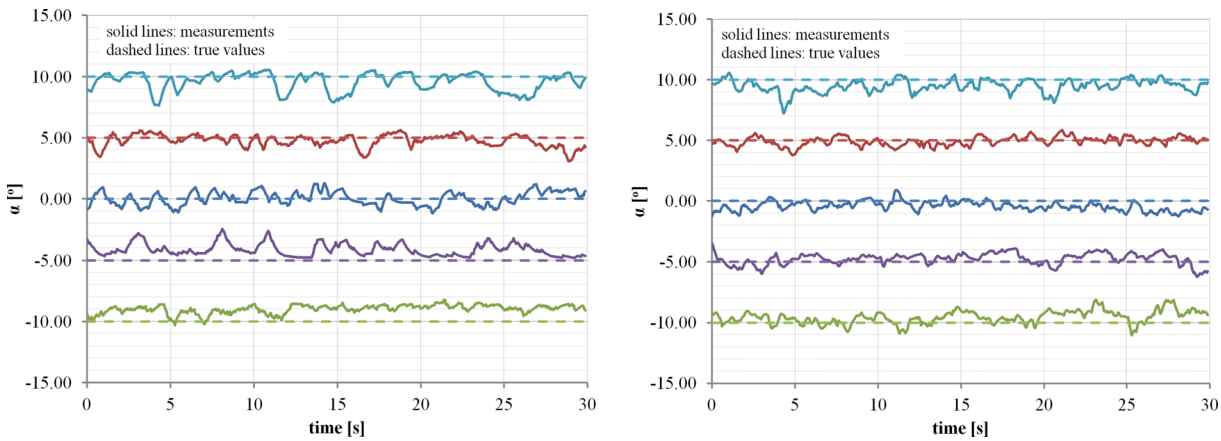

Fig. 10 Angle of attack validation at 12m/s airflow speed (*left*) and 20m/s speed (*right*)

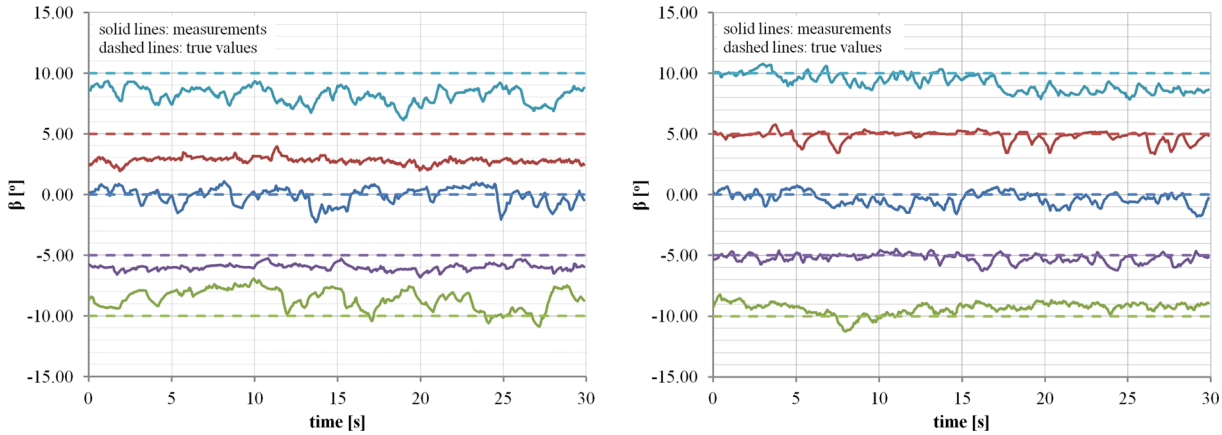

Fig. 11 Angle of sideslip validation at 12m/s airflow speed (*left*) and 20 m/s speed (*right*)

Figure 11 shows the validation results for the considered values of the sideslip with 0° angle of attack at 12 m/s and 20 m/s speeds. The samples of the measurement error are collected in the same way as in the angle of attack case. The measurement error in this case also tends to decrease as the airflow speed increases. The RMS is 0.92° at low speed and 0.54° at high speed. 67.9% of the samples lie within ±0.92° at low speed and 81.9% lie within ±0.54° at high speed. The 95% confidence intervals are [−1.37°, 1.37°] at low speed and [−0.79°, 0.79°] at high speed.

The probe is next tested in flight. The test entails maintaining the airplane in straight (and preferably level) flight, as sensor measurements, including those from the probe, are recorded. In this scenario, as long as the wind disturbances are relatively insignificant, the angle of attack should be approximately equal to the pitch angle minus the flight path angle. In our tests, we managed to maintain the airplane in almost level flight (i.e., at a roughly zero flight path angle). Figure 12 shows that the measured values of the angle of attack obtained from the probe correlate well with the measurements of the pitch angle from the AHRS sensor. Note that the 4° bias between the measurements from the probe and those from the AHRS is due to the fact that the probe is installed on the wing, which has an angle of incidence of approximately 4°. This type of test is not suitable for the validation of sideslip measurements due to the difficulties in flying an R/C airplane at a constant angle of sideslip.

3 UAV Platform Modeling

In order to design dynamically feasible trajectories offline and develop high-performance feedback controllers, a reasonably accurate model of the aircraft dynamics is required. A combination of semi-empirical, frequency domain, and time-domain identification techniques is utilized to obtain a mathematical representation of each major component of the system. This section is divided into five subsections: The first gives the equations of motion of the UAV; the second presents the test method used to determine the moments of inertia; the third describes the experiment conducted to obtain the frequency response of each actuator; the fourth focuses on the propeller thrust modeling; and the last subsection presents the parameter estimation process used for deriving the aerodynamic model of the UAV.

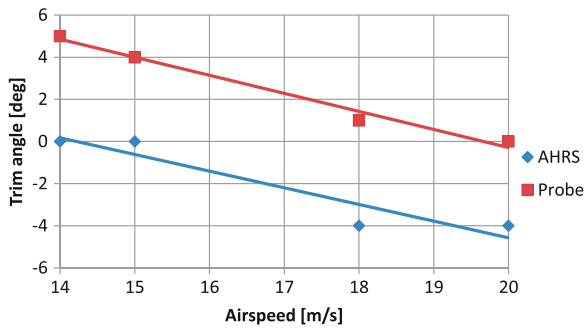

Fig. 12 In flight measurement of the angle of attack

3.1 Aircraft Equations of Motion

The dynamics of the UAV are described by standard rigid-body six-degree-of-freedom equations of motion in the aircraft body reference frame. Before giving these equations, we define the following reference frames:

$\{I\} :=$ inertial reference frame with X-axis pointing North, Y-axis pointing East, and Z-axis pointing down (NED)

$\{B\} :=$ body reference frame, fixed to the center of gravity of the UAV, with X-axis pointing to nose, Y-axis pointing to starboard wing, and Z-axis pointing down

The following notations are introduced to concisely present the equations of motion, as suggested by [7, 8, 27]:

$\mathbf{P} =$ position of the center of gravity in $\{I\} = [N,\ E,\ -H]^T$

$\mathbf{V} =$ linear velocity of the center of gravity relative to $\{I\}$, expressed in $\{B\} = [u,\ v,\ w]^T$

$\mathbf{V_w} =$ linear velocity of the wind relative to $\{I\}$, expressed in $\{B\} = [u_w,\ v_w,\ w_w]^T$

$\bar{\mathbf{V}} =$ linear velocity of the center of gravity relative to the wind, expressed in $\{B\} = \mathbf{V} - \mathbf{V_w} = [u - u_w, v - v_w, w - w_w]^T$

$V_a =$ airspeed of the unmanned aerial vehicle $= \sqrt{(u-u_w)^2 + (v-v_w)^2 + (w-w_w)^2}$

$\Omega =$ angular velocity of $\{B\}$ relative to $\{I\}$, expressed in $\{B\} = [p,\ q,\ r]^T$

$\Lambda =$ vector of Euler angles with respect to $\{I\} = [\phi,\ \theta,\ \psi]^T$, where ϕ denotes the bank (roll) angle, θ the elevation (pitch) angle, and ψ the heading (yaw) angle

${}^B_I\mathcal{R} =$ rotation matrix from $\{B\}$ to $\{I\}$ in SO(3), given in terms of Λ

$\mathbf{G} =$ gravitational acceleration vector expressed in $\{B\} = g[-\sin\theta, \cos\theta\sin\phi, \cos\theta\cos\phi]^T$, where g is the standard acceleration due to gravity

We assume the earth is flat and the gravity field is constant ($g = 9.80665\,\mathrm{m/s^2}$). Let $\boldsymbol{\delta} = [\delta_e,\ \delta_a,\ \delta_r,\ \delta_t]^T$, where δ_e, δ_a, and δ_r denote the elevator, aileron, and rudder deflections, respectively, and δ_t designates the throttle input. Note that these are the actual deflections, that is, the outputs of the servomotors used to deflect the control surfaces on the UAV. The commanded control surface deflections and throttle input, which are the inputs to the servomotors, are denoted by $\boldsymbol{\delta^c} = [\delta_e^c,\ \delta_a^c,\ \delta_r^c,\ \delta_t^c]^T$. The three servomotors used onboard the UAV are identical and each is modeled as a second-order system obtained by measuring the frequency response, as discussed in Section 3.3. We can then express the equations of motion as follows:

$$\begin{aligned}
\dot{\mathbf{V}} &= m^{-1}\mathbf{F}(\bar{\mathbf{V}}, \Omega, \boldsymbol{\delta}) + \mathbf{G} - \Omega \times \mathbf{V} \\
\dot{\Omega} &= \mathbf{J}^{-1}\mathbf{M}(\bar{\mathbf{V}}, \Omega, \boldsymbol{\delta}) - \mathbf{J}^{-1}\,(\Omega \times \mathbf{J}\Omega) \\
\dot{\mathbf{P}} &= {}^B_I\mathcal{R}(\Lambda)\mathbf{V} \\
\dot{\Lambda} &= \boldsymbol{\mathcal{E}}(\phi, \theta)\Omega
\end{aligned} \tag{5}$$

where $m = 3.24\,\mathrm{kg}$ is the mass of the UAV, $\mathbf{J}$ is the moment of inertia tensor, $\mathbf{F}(\bar{\mathbf{V}}, \Omega, \boldsymbol{\delta})$ denotes the aerodynamic and propulsion forces, $\mathbf{M}(\bar{\mathbf{V}}, \Omega, \boldsymbol{\delta})$ denotes the aerodynamic and propulsion moments, and

$$\boldsymbol{\mathcal{E}}(\phi, \theta) = \begin{bmatrix} 1 & \sin\phi\tan\theta & \cos\phi\tan\theta \\ 0 & \cos\phi & -\sin\phi \\ 0 & \sin\phi/\cos\theta & \cos\phi/\cos\theta \end{bmatrix},$$

$${}^B_I\mathcal{R}(\Lambda) = \begin{bmatrix} \cos\theta\cos\psi & \sin\phi\sin\theta\cos\psi - \cos\phi\sin\psi & \cos\phi\sin\theta\cos\psi + \sin\phi\sin\psi \\ \cos\theta\sin\psi & \sin\phi\sin\theta\sin\psi + \cos\phi\cos\psi & \cos\phi\sin\theta\sin\psi - \sin\phi\cos\psi \\ -\sin\theta & \sin\phi\cos\theta & \cos\phi\cos\theta \end{bmatrix}.$$

Note that, for some advanced control implementations, the use of quaternions instead of Euler angles would be more appropriate, especially when the maneuvers to be tracked stay in the gimbal lock region for a relatively long period of time (several time steps). However, as far as modeling is

concerned, the obtained aerodynamic model can still be used with equations of motion that include quaternion kinematics, and so, in this paper we will use the preceding equations of motion without loss of generality.

The ground testing procedures used to obtain the moments of inertia of the UAV, and hence the inertia tensor **J**, are described in Section 3.2. Sections 3.4 and 3.5 give the propulsion and aerodynamic models. Note that we assume the propeller does not significantly affect the airflow over the UAV. Consequently, we approach the aerodynamic and propulsion modeling separately. We can then write **F** and **M** as

$$\begin{aligned}\mathbf{F}(\bar{\mathbf{V}}, \Omega, \boldsymbol{\delta}) &= \mathbf{F_A}(\bar{\mathbf{V}}, \Omega, \delta_e, \delta_a, \delta_r) + \mathbf{F_P}(\bar{\mathbf{V}}, \delta_t),\\ \mathbf{M}(\bar{\mathbf{V}}, \Omega, \boldsymbol{\delta}) &= \mathbf{M_A}(\bar{\mathbf{V}}, \Omega, \delta_e, \delta_a, \delta_r) + \mathbf{M_P}(\bar{\mathbf{V}}, \delta_t),\end{aligned} \tag{6}$$

where $(\cdot)_{\mathbf{A}}$ and $(\cdot)_{\mathbf{P}}$ denote the aerodynamic and propulsion components, respectively.

3.2 Moments of Inertia

The moments of inertia of a full-scale aircraft about the roll and pitch axes are typically determined using the compound pendulum method, whereas the moment of inertia about the yaw axis is obtained using the bifilar pendulum approach, as described in [19, 33, 45]. In the case of a small UAV, the vehicle can be easily tilted sideways, and so the moment of inertia about the yaw axis can also be determined using the compound pendulum method. That way, the same setup can be used to perform all the experiments. The bifilar pendulum method can also be used to determine all the moments of inertia of a small UAV, as shown, for example, in [23], provided that the testing setup is appropriately configured to avoid the inadvertent excitation of the swaying mode, which could otherwise result in significant measurement errors as discussed in [28]. Thus, either of the aforementioned test methods can be used to compute the moments of inertia of a small UAV. In our case, we have used the compound pendulum method simply for convenience.

The moments of inertia about the roll, pitch, and yaw axes are determined in three separate experiments. In each experiment, the UAV is positioned appropriately on a wire suspended cradle, as shown in Fig. 13, in order to obtain the moment of inertia about the desired axis. The experiment entails finding the oscillation period of the pendulum and then computing from this period the moment of inertia by applying a simple mathematical formula. It is indicated in [33] and observed in our preliminary tests that the compound pendulum method is sensitive to the length of the suspending wires. Specifically, the accuracy of the measurements obtained using this method degrades as the distance from the pivot axis of the pendulum to the center of gravity of the UAV, denoted by L, increases. This finding can also be verified by examining the mathematical formula used to compute the moment of inertia and doing some sensitivity analysis. The formula for computing the moment of inertia, $\mathcal{I}$, is based on the linearized equation of motion of the compound pendulum and is given by $\mathcal{I} = \dfrac{mgLT^2}{4\pi^2} - mL^2$, where T is the oscillation period of the pendulum, g is the acceleration due to gravity, and L is as defined before. As the major source of error in computing the moment of inertia is the inaccuracy in the measurement of the oscillation period, it is important to examine the local sensitivity of $\mathcal{I}$ with respect to T. Suppose that the true value of the moment of inertia is $\mathcal{I}_n$, and the corresponding oscillation period is T_n. Then, the local sensitivity of $\mathcal{I}$ with respect to T is $\dfrac{\partial \mathcal{I}}{\partial T} = \dfrac{1}{\pi}\sqrt{mgL\left(\mathcal{I}_n + mL^2\right)}$. It is clear from the preceding equation that, as L increases, any small discrepancy in the period measurement would yield a more significant error in the computation of the moment of inertia.

As mentioned before, the test setup for determining the moments of inertia is shown in Fig. 13. The cradle that holds the vehicle is connected to the pivot points on the ceiling by four braided steel wires. The cradle consists of a wooden frame, along with four eyescrews to attach the frame to the steel wires. The cradle is located at 1.18 m from the pivot axis and has a mass of 1.27 kg. When placing the vehicle on the cradle, it is important to make sure that the center of gravity of the vehicle is as close as possible to the center of the cradle. The test setup does not require any specific mounting apparatus, and therefore can be used for multiple airplane models of similar size. Prior to the testing of the UAV, a calibration test is performed to determine the moment of inertia of the cradle, following the standard compound pendulum procedure. The moment of inertia of the cradle about the pivot axis is found to be 1.96 kg m^2. Three experiments are

Fig. 13 Moments of inertia testing setup: wire suspended cradle (*left*); setup to determine the moment of inertia about the pitch axis (*top middle*), the roll axis (*bottom middle*), and the yaw axis (*right*)

then performed to determine the moments of inertia of the UAV about the roll, pitch, and yaw axes (X, Y, and Z axes in the body reference frame), which are denoted by $\mathcal{I}_{xx}$, $\mathcal{I}_{yy}$, and $\mathcal{I}_{zz}$, respectively. The location of the center of gravity of the UAV in each of these experiments slightly changes based on the orientation of the airplane with respect to the cradle. These locations, measured from the pivot axis of the pendulum, are 1.22, 1.35, and 1.21 m corresponding to the configurations used to determine $\mathcal{I}_{xx}$, $\mathcal{I}_{yy}$, and $\mathcal{I}_{zz}$, respectively. The mass of the UAV is 3.24 kg and is slightly increased to 3.31 kg when determining $\mathcal{I}_{xx}$ due to the addition of a wooden bar to hold the airplane in place during this test.

To determine the moment of inertia about a specific axis of the UAV, the compound pendulum test is repeated 3 times. In each of these tests, the time required to complete 50 oscillations is recorded. Then, the average of the three recorded values, denoted by T_{50}, is used to compute the moment of inertia by applying the following equation:

$$\mathcal{I}_2 = \frac{g(m_1 L_1 + m_2 L_2)}{\omega_n^2} - \mathcal{I}_1 - m_2 L_2^2,$$

where $\omega_n = 100\pi / T_{50}$ is the frequency of oscillation, m_1 is the mass of the cradle, m_2 is the mass of the UAV, L_1 is the location of the center of gravity of the cradle, L_2 is the location of the center of gravity of the UAV (both locations measured from the pivot axis), $\mathcal{I}_1$ is the moment of inertia of the cradle about the pivot axis, and $\mathcal{I}_2$ is the moment of inertia of the UAV about its body axis. Table 3 gives the calculated values of the moments of the inertia of the UAV. Concerning the computation of the inertia tensor **J**, it is reasonable to assume in our case that the "cross-product-of-inertia" terms, $\mathcal{I}_{xy}$, $\mathcal{I}_{xz}$, and $\mathcal{I}_{yz}$, are all zeros, and hence, we have

$$\mathbf{J} = \begin{bmatrix} \mathcal{I}_{xx} & -\mathcal{I}_{xy} & -\mathcal{I}_{xz} \\ -\mathcal{I}_{xy} & \mathcal{I}_{yy} & -\mathcal{I}_{yz} \\ -\mathcal{I}_{xz} & -\mathcal{I}_{yz} & \mathcal{I}_{zz} \end{bmatrix} = \begin{bmatrix} 0.21 & 0 & 0 \\ 0 & 0.31 & 0 \\ 0 & 0 & 0.48 \end{bmatrix}.$$

3.3 Servo Model

Three servomotors are used to deflect the control surfaces on the UAV. These servos are identical and their dynamics are described by the same second-order system model. For instance, the system equations of the servo used to deflect the elevator are:

$$\begin{bmatrix} \dot{x}_{1s} \\ \dot{x}_{2s} \\ \hline \delta_e \end{bmatrix} = \left[\begin{array}{cc|c} 0 & 1 & 0 \\ -\omega_{ns}^2 & -2\zeta_s\omega_{ns} & \omega_{ns}^2 \\ \hline 1 & 0 & 0 \end{array}\right] \begin{bmatrix} x_{1s} \\ x_{2s} \\ \hline \delta_e^c \end{bmatrix}, \tag{7}$$

where x_{1s} and x_{2s} are the internal states of the servo, δ_e^c is the commanded elevator deflection, δ_e is the actual deflection, ω_{ns} is the natural frequency of the servo mechanism, and ζ_s is the damping ratio.

This model, and specifically the natural frequency and damping ratio of the servo, are obtained experimentally by measuring the frequency response. The

Table 3 Moments of inertia of the Telemaster UAV

	$\mathcal{I}_{xx}$	$\mathcal{I}_{yy}$	$\mathcal{I}_{zz}$	
T_{50}	114.89	118.25	115.36	s
ω_n	2.73	2.66	2.72	rad/s
$\mathcal{I}$	0.21	0.31	0.48	kgm^2

frequency response test is performed by sending continuous sinusoidal command inputs at different frequencies to the servo, one at a time, and, in each case, recording the commanded signal and the corresponding response simultaneously. The frequencies are chosen to cover a wide range about the cutoff frequency of the servo. The test setup is given in Fig. 14.

To measure the servo response, a potentiometer is mounted such that the shaft of the potentiometer is aligned with that of the servo. This potentiometer is supplied with 5 V voltage by an Ardupilot board and produces $0 - 5$ V output based on the angular position of its shaft. The Ardupilot is also used to generate the reference command and send it to the servo, as well as record the output from the potentiometer. The potentiometer readings for a number of commanded servo positions are recorded prior to the frequency response test in order to determine the calibration curve for this sensor. At each test frequency, the magnitude and phase shift of the frequency response are determined by comparing the commanded input sinusoid and the measured steady-state output signal; the values obtained are given in Table 4.

Frequency domain fitting is applied to the test data, with the natural frequency and damping ratio used as the fitting parameters. Since the system is fairly simple, the natural frequency and damping ratio are adjusted manually to obtain a satisfactory fit. A natural frequency of $\omega_{ns} = 13.7$ rad/s and a damping ratio of $\zeta_s = 0.67$ are obtained for the Futaba S3152 servo used in this work. The test data in Table 4 and the second-order system fit are shown in Fig. 15.

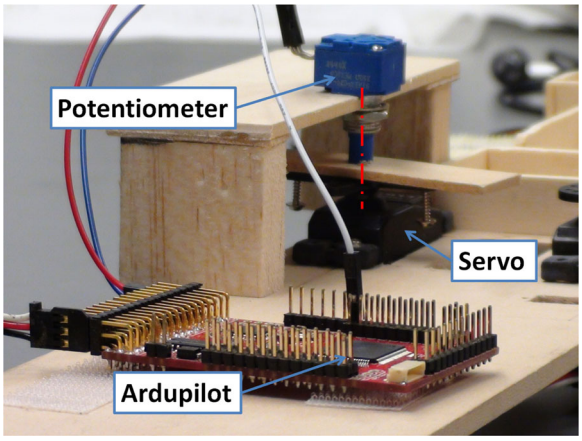

Fig. 14 Test setup for the frequency domain identification of the Futaba S3152 servo model

Table 4 Futaba S3152 frequency response

Frequency Hz	Magnitude -	Phase rad
0.01	1.00	0.00
0.10	1.00	-0.04
1.00	0.96	-0.57
2.00	0.81	-1.51
4.00	0.31	-3.02
5.00	0.19	-3.14

3.4 Propulsion Model

The propulsion system of the Telemaster UAV consists of a 760 RPM/Volt electric motor and a 13 × 8 inch propeller. The engine is powered by a 3S LiPo battery and controlled by a 40 Amps speed controller. We now derive a propulsion model of our system. We assume the propeller axis to be perfectly aligned with the body X-axis. As a result, the propeller thrust will be applied along the body X-axis only, that is, $\mathbf{F_P}(\bar{\mathbf{V}}, \delta_t) = [F_{PX}(V_a, \delta_t),\ 0,\ 0]^T$, and further, the thrust will not generate any moments, namely $\mathbf{M_P}(\bar{\mathbf{V}}, \delta_t) = 0$. The propulsion system model maps the throttle command δ_t, which is a PWM (pulse-width modulation) signal, to the generated propeller thrust $F_{PX}(V_a, \delta_t)$, given a certain airspeed. We assume that the dynamics of the propulsion system are fast enough that we may ignore the transient behavior. We also assume that,

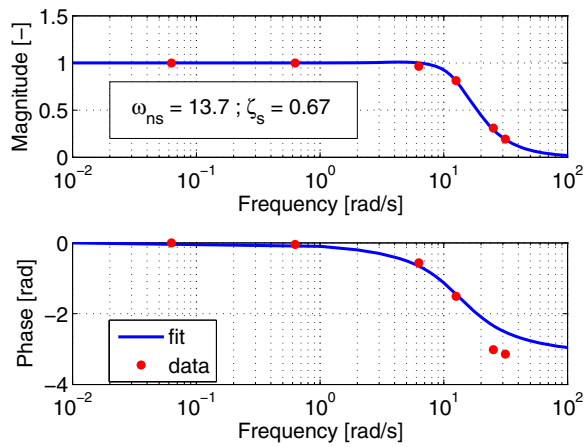

Fig. 15 Curve fitting of the servo test data

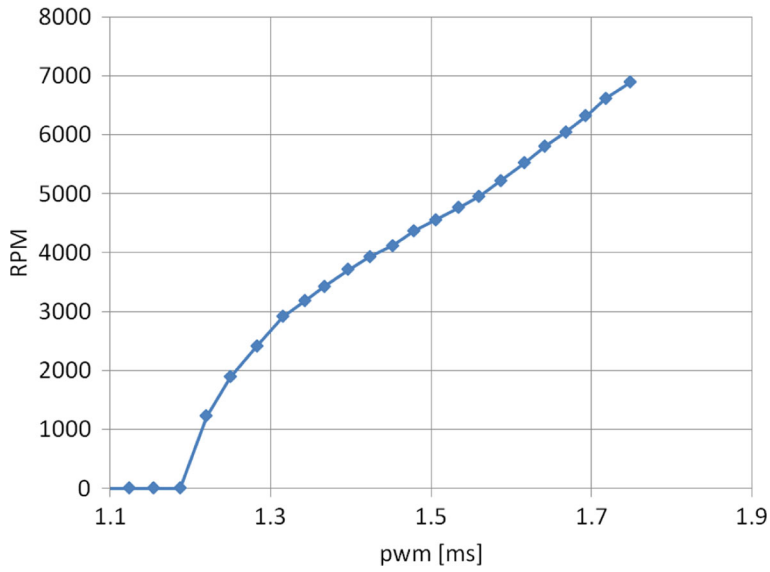

Fig. 16 Relationship between the throttle command δ_t, which is a PWM signal, and the engine RPM

even under nonzero airspeed conditions, the electronic speed controller (ESC) is able to ensure that, for a constant throttle command, the engine runs at a constant RPM.

We have obtained experimentally a look-up table, represented graphically in Fig. 16, that can be used to map a throttle command into the corresponding engine RPM through interpolation. Then, given the engine RPM and the current airspeed, we can compute the generated propeller thrust using look-up tables obtained from the propeller analysis applet, Javaprop [21]. This applet uses blade element theory to return a thrust profile based on the propeller geometry. The complete thrust model, which relates the engine RPM and airspeed to propeller thrust, is given in Fig. 17. Notice that, for a propeller rotating at a constant RPM, increasing the airspeed decreases the effective angle of attack of the propeller blade and, as a result, decreases the propeller thrust. Increasing the airspeed beyond a certain value will reverse the effective angle of attack, and hence cause the propeller to generate drag instead of thrust. From this figure, we also observe that the

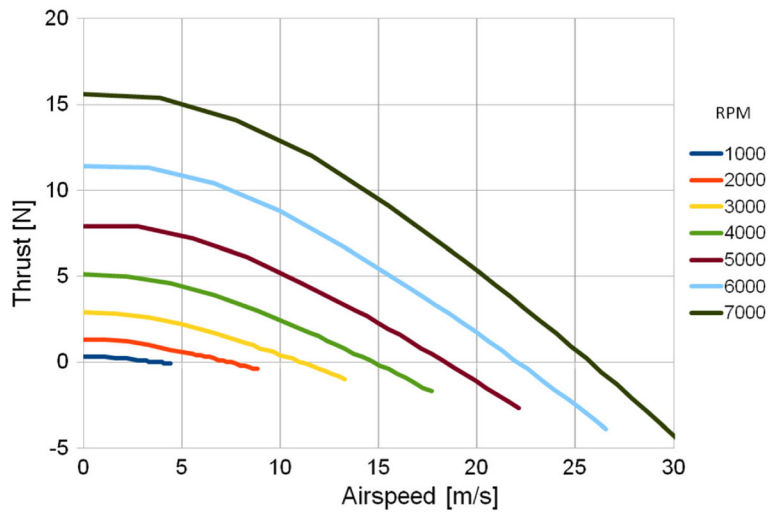

Fig. 17 Thrust prediction as a function of airspeed and engine RPM (Javaprop)

maximum thrust-to-weight ratio of the Telemaster is about 0.41, which is a typical value for a trainer class R/C airplane.

The thrust predictions generated by Javaprop at zero airspeed (static data) are verified through ground testing. The test setup is given in Fig. 18, which shows the engine mounted on an apparatus that is attached to a weight scale, with the propulsion system set up in a pusher configuration, that is, the generated thrust pushes the whole test apparatus downward. We use the weight scale and a tachometer to obtain the values of the propeller thrust and engine RPM, respectively, for each considered throttle setting. The static thrust data returned by Javaprop and those obtained from two ground tests, performed using two different batteries, are given in Fig. 19. The figure clearly shows that the Javaprop predictions closely match the static test data.

3.5 Aerodynamic Model

The goal of aerodynamic modeling is to obtain a reasonably accurate mapping from the airplane state and control variables to the aerodynamic forces and moments in the operating envelope (which is generally defined using altitude and airspeed limits). Thus, we need to find formulas for $\mathbf{F_A}(\bar{\mathbf{V}}, \Omega, \delta_e, \delta_a, \delta_r) = [F_X, \ F_Y, \ F_Z]^T$ and $\mathbf{M_A}(\bar{\mathbf{V}}, \Omega, \delta_e, \delta_a, \delta_r) = [M_X, \ M_Y, \ M_Z]^T$, as defined in Eq. 6, where F_i is the component of the aerodynamic force in the body i-axis and M_i is the aerodynamic moment about the body i-axis. Specifically, we aim to determine the force coefficients $C_i = F_i/(Q\,S)$, for $i = X, Y, Z$, and the moment coefficients $C_l = M_X/(Q\,S\,b)$, $C_m = M_Y/(Q\,S\,\bar{c})$, and $C_n = M_Z/(Q\,S\,b)$, where $Q = 0.5\,\rho\,V_a^2$ is the dynamic pressure, with ρ being the air density, S is the wing area, b is the wing span, and $\bar{c}$ is the mean aerodynamic chord. The values of the aforementioned geometrical parameters can be found in Table 1.

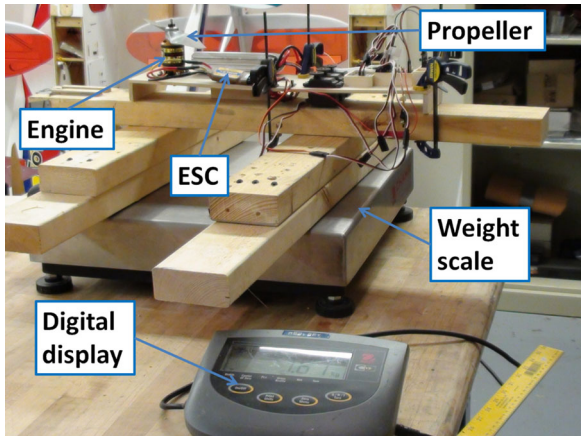

Fig. 18 Test setup for measuring propeller thrust at zero airspeed

The aerodynamic model can be obtained using several methods, including those based on semi-empirical techniques, computational fluid dynamics (CFD), wind tunnel testing, and flight testing. A semi-empirical method typically uses basic aerodynamic theories, along with some experimental data, to generate an aerodynamic model based on some geometrical parameters of the airplane. There are available software, such as digital DATCOM [51], which use semi-empirical methods to predict the aerodynamic characteristics of an airplane. DATCOM, in particular, takes some geometrical parameters as inputs and outputs aerodynamic coefficients and stability derivatives. Applying such methods to find aerodynamic models for small UAVs may be unfavorable in general because most of the experimental data used by these methods are obtained for full-scale aircraft. There are several, freely available, linear CFD codes based on vortex lattice analysis, such as Athena Vortex Lattice [31] and Tornado [48], that can be used to develop aerodynamic models for small UAVs. The CFD approach generally gives a satisfactory aerodynamic model in the linear region of the aerodynamic force and moment curves. However, this approach does not take into account the effects of gaps between the control surfaces and the wings or tails in computing the forces and moments generated by the control surface deflections. The drag prediction is also optimistic in this case, that is, the resulting model underestimates the value of drag; the reason is the CFD method only considers the drag generated by the pressure distribution around the wings and fuselage and neglects the drag due to skin friction and appendices such as the landing gear. Wind tunnel testing offers accurate and comprehensive aerodynamic data to develop a high-fidelity model, but this comes at the expense of high cost and relatively long model development time [5]. In the case of small, low-cost UAVs, the cost and time to perform the necessary wind tunnel tests can be prohibitive. System identification and/or parameter estimation techniques can

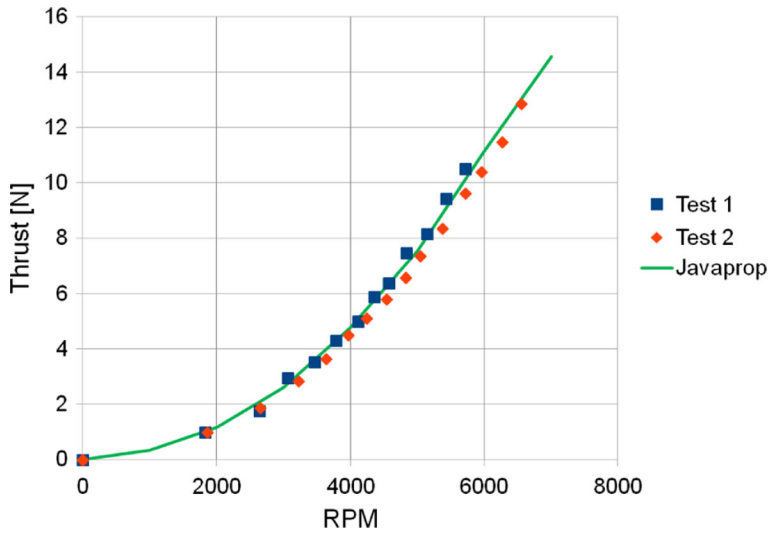

Fig. 19 Static thrust data along with Javaprop predictions

be used to develop aerodynamic models from flight test data [24, 29, 47]. The structure of the aerodynamic model may be determined based on the test data by using, for instance, a stepwise regression method (system identification), or it can be simply postulated. Parameter estimation techniques can then be used to estimate the values of the aerodynamic coefficients.

In this paper, the aerodynamic model is obtained from flight test data using the output error method for parameter estimation in the time domain. The output error method is a maximum likelihood estimator for data with measurement noise [16]. This method is asymptotically unbiased and consistent, that is, the estimated parameters will approach their true values as the number of measurements increases [29]. It is computationally manageable, especially when compared to the more sophisticated filter error method [24]. But, unlike the filter error method, the output error approach is not well-suited to handling process noise, and so it is important to carry out the flight tests in the absence of significant atmospheric disturbances. Details on the use of the output error method for aerodynamic parameter estimation can be found in [24, 29]. The structure of the aerodynamic model used is given in Eq. 8, as suggested in [43]. This structure is chosen so that a single model can be used to capture the UAV dynamics in the entire operating envelope of interest.

$$
\begin{aligned}
C_X &= C_{X_0} + C_{X_\alpha}\alpha + C_{X_{\alpha^2}}\alpha^2 \\
C_Y &= C_{Y_0} + C_{Y_\beta}\beta + C_{Y_p}\frac{p\,b}{2V_a} + C_{Y_r}\frac{r\,b}{2V_a} \\
&\quad + C_{Y_{\delta a}}\delta_a + C_{Y_{\delta r}}\delta_r \\
C_Z &= C_{Z_0} + C_{Z_\alpha}\alpha + C_{Z_{\delta e}}\delta_e + C_{Z_{\alpha^2}}\alpha^2 \\
C_l &= C_{l_0} + C_{l_\beta}\beta + C_{l_p}\frac{p\,b}{2V_a} + C_{l_r}\frac{r\,b}{2V_a} \\
&\quad + C_{l_{\delta a}}\delta_a + C_{l_{\delta r}}\delta_r \\
C_m &= C_{m_0} + C_{m_\alpha}\alpha + C_{m_q}\frac{q\,\bar{c}}{2V_a} + C_{m_{\delta e}}\delta_e \\
&\quad + C_{m_{\alpha^2}}\alpha^2 \\
C_n &= C_{n_0} + C_{n_\beta}\beta + C_{n_p}\frac{p\,b}{2V_a} + C_{n_r}\frac{r\,b}{2V_a} \\
&\quad + C_{n_{\delta a}}\delta_a + C_{n_{\delta r}}\delta_r
\end{aligned}
\tag{8}
$$

The flight tests for parameter estimation in our case are performed by a pilot on the ground controlling the airplane remotely. Hence, only a few standard maneuvers for parameter estimation can be successfully performed. These maneuvers capture the dutch-roll, bank-to-bank, and short period motions of the aircraft. Specifically, we employ standard control input patterns for time-domain parameter estimation [24] to

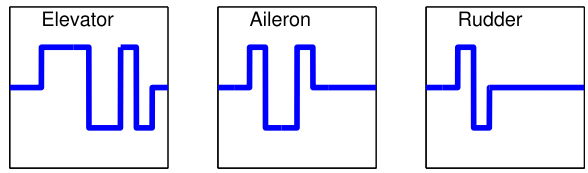

Fig. 20 Control input shapes for parameter estimation

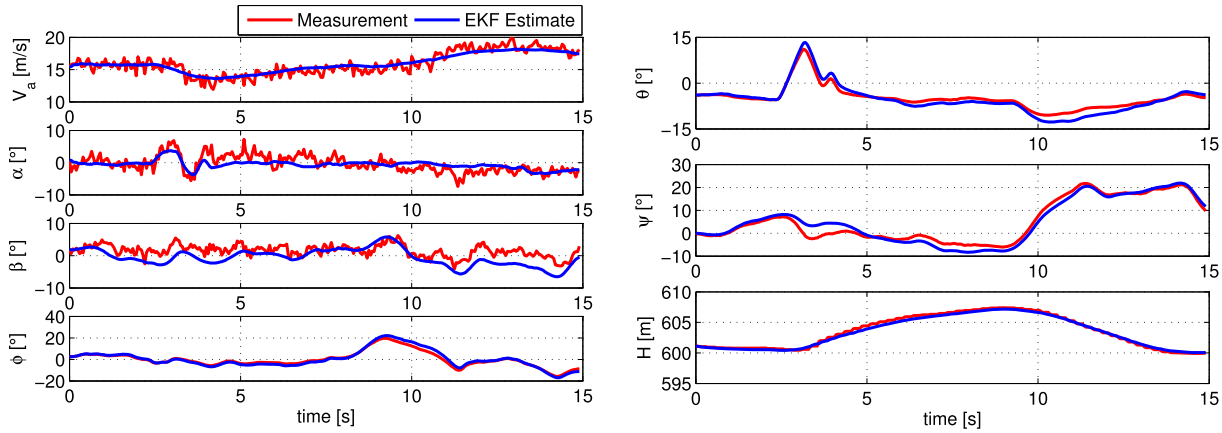

Fig. 21 Data compatibility check using EKF prior to parameter estimation

excite the vehicle. The input patterns used are different for each control actuator: doublet inputs are used for the rudder to capture the dutch-roll mode, 1-2-1 for the aileron to capture the bank-to-bank motion, and 3-2-1-1 for the elevator to capture the short period mode. These integers indicate the number of time steps to hold a control actuator at a specified position before moving it to the same position in the opposite direction. Figure 20 illustrates the shape of each control surface input to be executed during the flight tests. In this figure, the time step Δt and the magnitude of the deflection are chosen such that the control input sufficiently excites the airplane (namely, generate $0.4 - 0.5\,g$ acceleration) without causing it to deviate significantly from the nominal flight condition. The guideline for choosing the best input is provided by [24], which is based on the frequency of the aircraft mode of interest. For the aircraft used in this work, the time step Δt is chosen to be equal to 250 ms, and an appropriate magnitude of the control surface deflection is determined during the flight tests. To maintain consistency between tests, the onboard computer is used to generate the commands for control surface deflections from the trim condition.

Prior to estimating the aerodynamic model parameters, a compatibility check is performed on the test data. The objective of this step is twofold: first, to ensure that the data satisfies the kinematic relationships dictated by the equations of motion, and second, to estimate and remove any bias and scale factor errors in the measured data. An Extended Kalman Filter (EKF) is used to obtain an estimate of the time history of the vector-valued function $\mathbf{x} = [u,\ v,\ w,\ \phi,\ \theta,\ \psi]^T$, as well as determine any sensor

Table 5 Estimated measurement biases and scales

bias	value	unit	scales	value
B_{ax}	-0.0434	m/s	K_{ax}	1.0000
B_{ay}	0.1200	m/s	K_{ay}	1.0000
B_{az}	-0.0097	m/s	K_{az}	1.0000
B_p	-0.0011	rad/s	K_p	1.0000
B_q	-0.0032	rad/s	K_q	1.0000
B_r	-0.0082	rad/s	K_r	1.0000
B_{Va}	-0.0199	m	K_{Va}	1.0000
B_α	0.0587	rad	K_α	1.0000
B_β	0.0118	rad	K_β	1.0000

Table 6 Estimated parameters

Parameter	Value	Parameter	Value	Parameter	Value
C_{X_0}	-0.1004	C_{Y_0}	+0.0446	C_{Z_0}	-0.4522
C_{X_α}	-0.0928	C_{Y_β}	-0.5724	C_{Z_α}	-5.3550
$C_{X_{\alpha^2}}$	+1.7729	C_{Y_p}	+0.1203	$C_{Z_{\alpha^2}}$	-4.3813
		C_{Y_r}	+0.1181	$C_{Z_{\delta e}}$	+0.7406
		$C_{Y_{\delta a}}$	-0.0276		
		$C_{Y_{\delta r}}$	+0.1584		
Parameter	Value	Parameter	Value	Parameter	Value
C_{l_0}	+0.0128	C_{m_0}	-0.0057	C_{n_0}	-0.0068
C_{l_β}	-0.0579	C_{m_α}	-0.2402	C_{n_β}	+0.0538
C_{l_p}	-0.3590	$C_{m_{\alpha^2}}$	-0.0750	C_{n_p}	-0.0489
C_{l_r}	+0.1420	C_{m_q}	-10.6607	C_{n_r}	-0.0831
$C_{l_{\delta a}}$	+0.1519	$C_{m_{\delta e}}$	+0.5737	$C_{n_{\delta a}}$	-0.0139
$C_{l_{\delta r}}$	+0.0042			$C_{n_{\delta r}}$	-0.0465

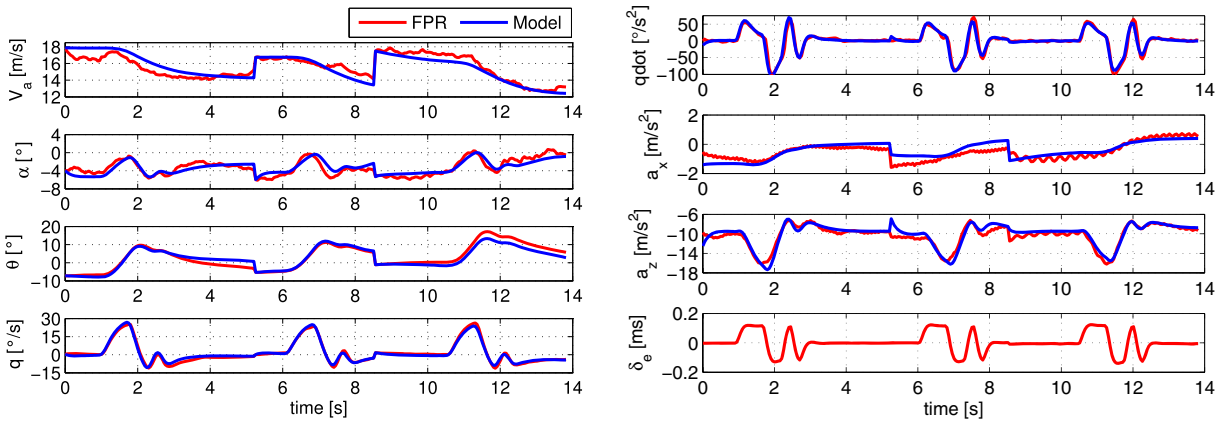

Fig. 22 Comparison of reconstructed flight test data (through FPR process) and model response: longitudinal parameter estimation run; the elevator deflection, δ_e, from the flight test is used to drive the simulation process

bias and scale factor errors. This process, referred to as flight path reconstruction (FPR) [24, 29, 37], utilizes the first and last equations from Eq. 5 with the adjusted measurements of the linear accelerations, a_x, a_y, and a_z, and the angular rates, p, q, and r, as inputs to the system. The notations a_x, a_y, and a_z denote the linear accelerations at the center of gravity of the UAV along the body X, Y, and Z axes, respectively. These accelerations are not measured directly, but can be obtained from those given by the AHRS as follows: $[a_x, a_y, a_z]^T = m^{-1}\mathbf{F}(\bar{\mathbf{V}}, \Omega, \boldsymbol{\delta}) = [\hat{a}_x, \hat{a}_y, \hat{a}_z]^T - \Omega \times (\Omega \times \Delta\mathbf{P}) - \dot{\Omega} \times \Delta\mathbf{P}$, where $\Delta\mathbf{P}$ is the position of the AHRS (which is located on the body X-axis) relative to the center of gravity of the UAV, $\hat{a}_x$, $\hat{a}_y$, and $\hat{a}_z$ are measured by the AHRS and denote the linear accelerations at the location of the AHRS, expressed in $\{B\}$, and the derivative $\dot{\Omega}$ is computed in our case using the central difference method. Aside from the aforementioned inputs, the EKF uses measurements of ϕ, θ, ψ (given by the AHRS) and V_a, α, β (given by the airdata probes) to update the state estimates. Note that $\alpha = \tan^{-1}((w - w_w)/(u - u_w))$ and $\beta = \sin^{-1}((v - v_w)/V_a)$. As all of the data to be used in the parameter estimation are obtained from several tests performed during a single flight, it is sensible to process all the test data simultaneously in order to obtain a single set of values for bias and scale factor errors. To process the data concurrently, the EKF is modified to expand the number of states and measurements following the addition of flight test data to the FPR process. That is,

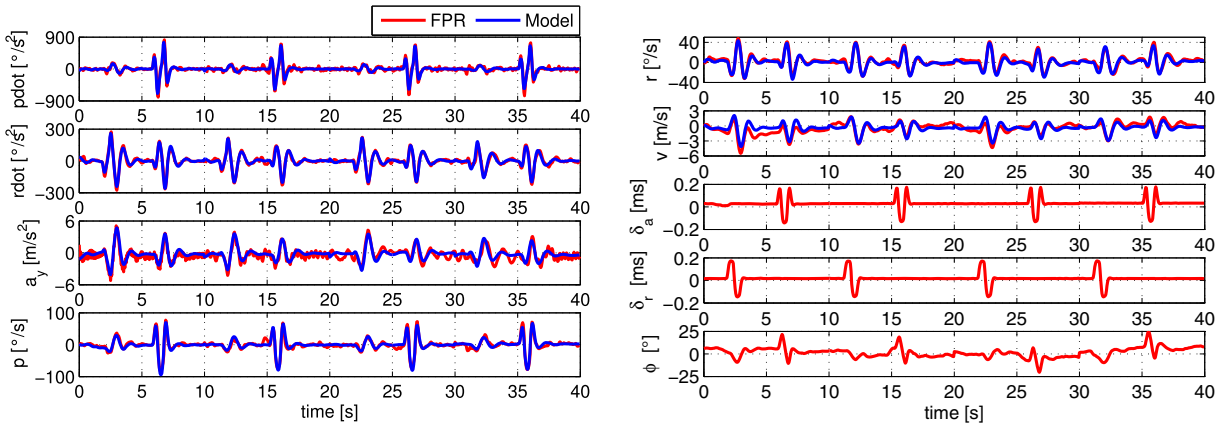

Fig. 23 Comparison of reconstructed flight test data (through FPR process) and model response: lateral-directional parameter estimation run; the reconstructed bank angle (ϕ) data, along with the aileron (δ_a) and rudder (δ_r) deflections applied in the flight test, are used to drive the simulation process

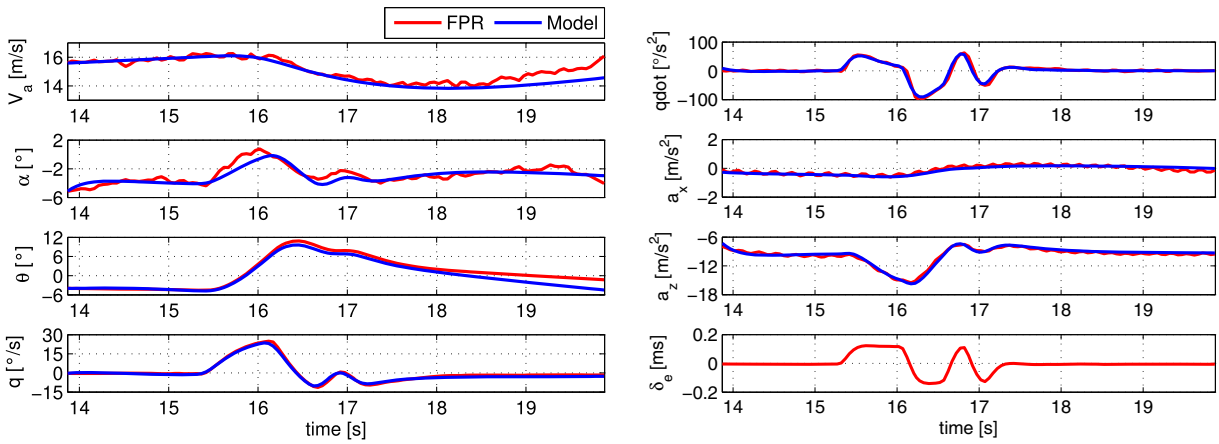

Fig. 24 Comparison of reconstructed flight test data (through FPR process) and model response: longitudinal model validation run

for each flight test i, we add dynamic equations to the EKF (the first and last equations from Eq. 5), along with the measurements from this run, to estimate the time history of the corresponding vector-valued function $\mathbf{x}^{(i)}$. We incorporate sensor bias and scale factor errors in the measurement equations for $\hat{a}_x$, $\hat{a}_y$, $\hat{a}_z$, p, q, r, V_a, α, and β, which take the form: $R = K_R R_m - B_R$, where R is the adjusted value of the variable being measured, R_m is the measured value given by the sensor, K_R is the scale factor error, and B_R is the measurement bias. We use the procedure outlined in [17] to design the EKF. The measurement and discrete state noise covariance matrices, as well as the initial value of the state covariance matrix, are all chosen to be constant and diagonal, with the values of the diagonal entries selected appropriately based on several iterations and some known characteristics such as the variances of the measurements in the case of the measurement covariance matrix.

A comparison of the raw and reconstructed data for an elevator 3-2-1-1 test is given in Fig. 21. For the test data used to derive the aerodynamic model, the bias terms and scale factors are not significant, with the exception of the angle of attack measurement bias, B_α, as shown in Table 5. The larger bias in the angle of attack measurements is a consequence of the airdata probe being installed parallel to the bottom surface of the wing, which has a 4° incidence angle from the body X-axis.

It is convenient to decouple the estimation of the longitudinal and lateral-directional parameters [24]. This decoupling is acceptable under the assumption that, when the aircraft is in steady symmetric level flight, a small perturbation in the longitudinal motion

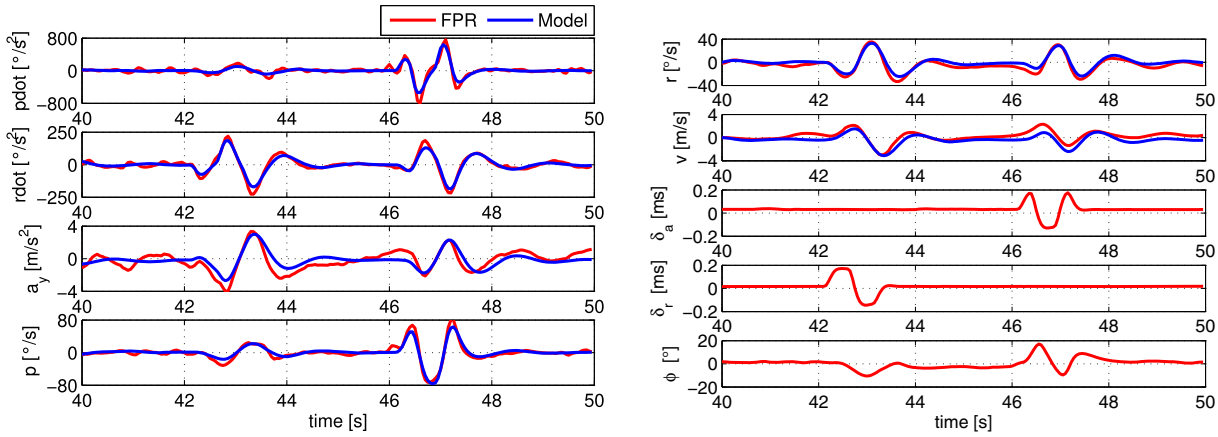

Fig. 25 Comparison of reconstructed flight test data (through FPR process) and model response: lateral-directional model validation run

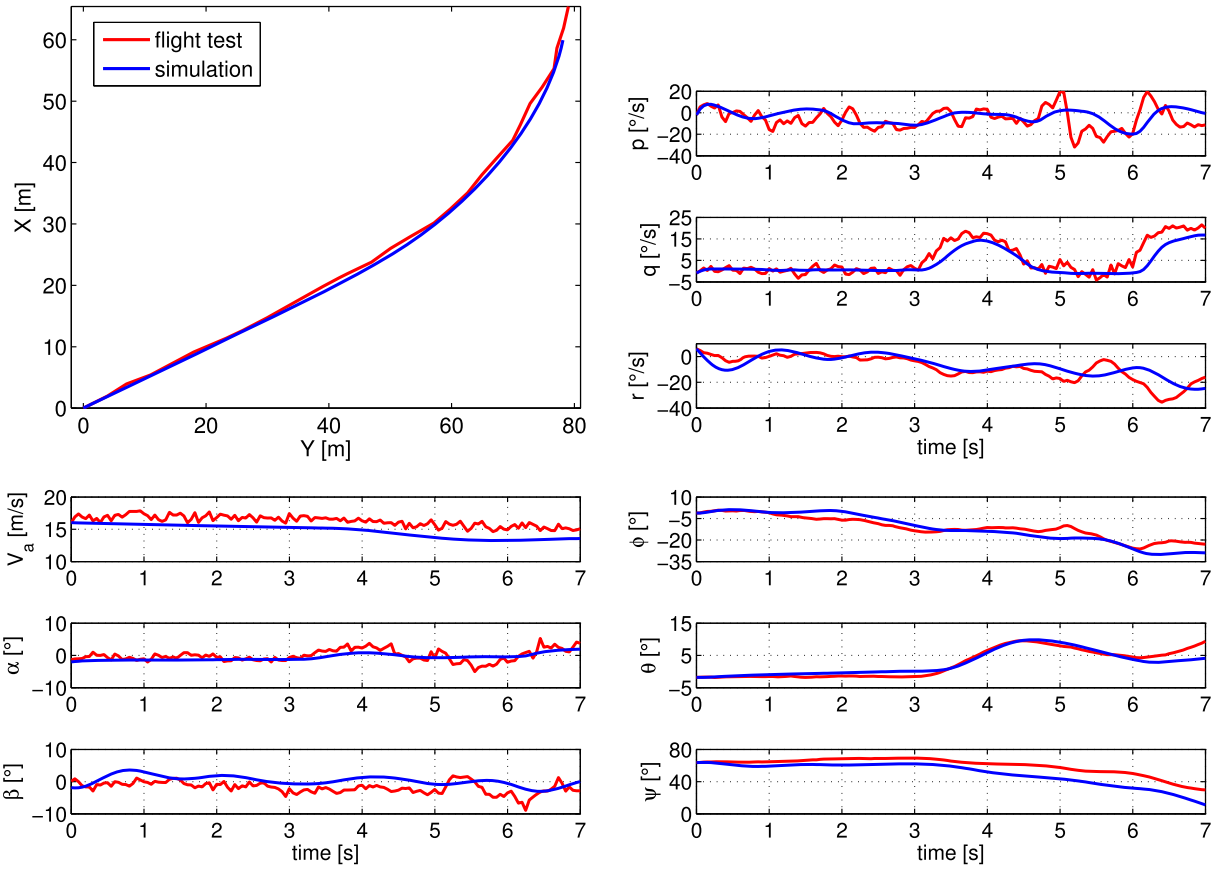

Fig. 26 Comparison of simulated and measured responses: a gentle left turn maneuver

will not affect the lateral-direction motion and vice versa. In general, this scenario is difficult to achieve in the case of a small UAV because of the imperfections in the aircraft and the difficulty for an on-ground pilot to ensure a steady symmetric level flight. To circumvent these issues, multiple tests are performed at similar flight conditions. These tests are subsequently analyzed and those which satisfy the steady symmetric level flight requirement are then used in the parameter estimation process.

We have used three flight test runs to estimate the longitudinal aerodynamic parameters and four test runs to estimate the lateral-directional parameters. The estimated parameters are given in Table 6. Figures 22 and 23 show that the output of the estimated model matches well both the longitudinal and lateral-directional test data. Note that, in all the relevant figures, the elevator, aileron, and rudder deflections, which are PWM signals, are given in terms of the deviations from a reference value of 1.5 ms, which corresponds to approximately zero deflection. The estimated aerodynamic parameters are validated against flight test data that are not included in the parameter estimation process. Specifically, the inputs from this data, that is, the control surface deflections and initial conditions, are used to drive a simulated model that uses the values of the aerodynamic coefficients identified in the estimation process. The simulated response is then compared to the measured response to see how well the estimated aerodynamic model parameters are able to predict the response of the actual airplane. A comparison of the predicted and measured responses is given in Figs. 24 and 25 for the longitudinal and lateral-directional tests, respectively. The response of the simulated system is fairly close to the measured response, which indicates that the obtained model adequately captures the aircraft dynamics at the test conditions.

In the following, we examine how closely the derived flight dynamic model describes the behavior

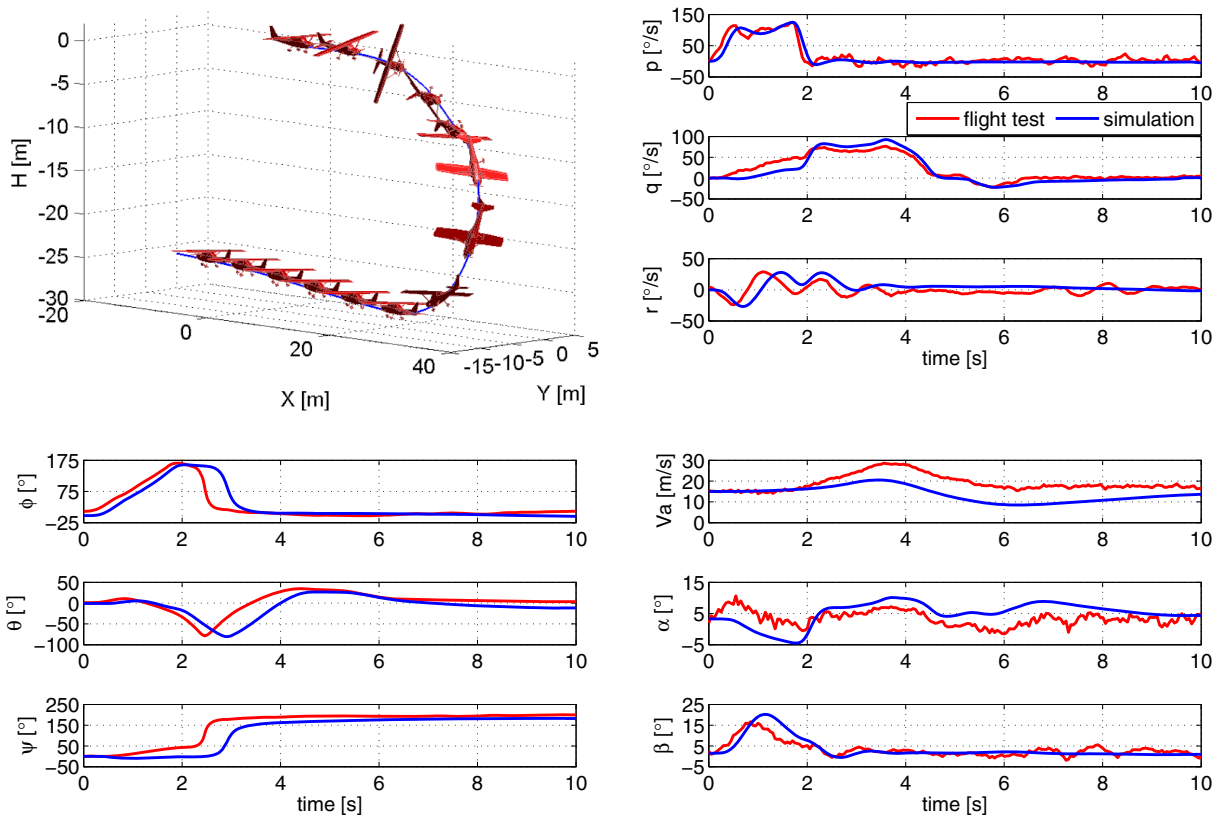

Fig. 27 Comparison of simulated and measured responses: a Split-S maneuver

of the UAV given certain commanded control inputs. We first consider recorded flight test data corresponding to a gentle left turn maneuver. As evident from Fig. 26, the simulated trajectory captures most of the features of the actual flight trajectory. The same observation holds for the case where the UAV executes a Split-S maneuver, as can be ascertained from Fig. 27. We have also synthesized a linear time-invariant H_∞

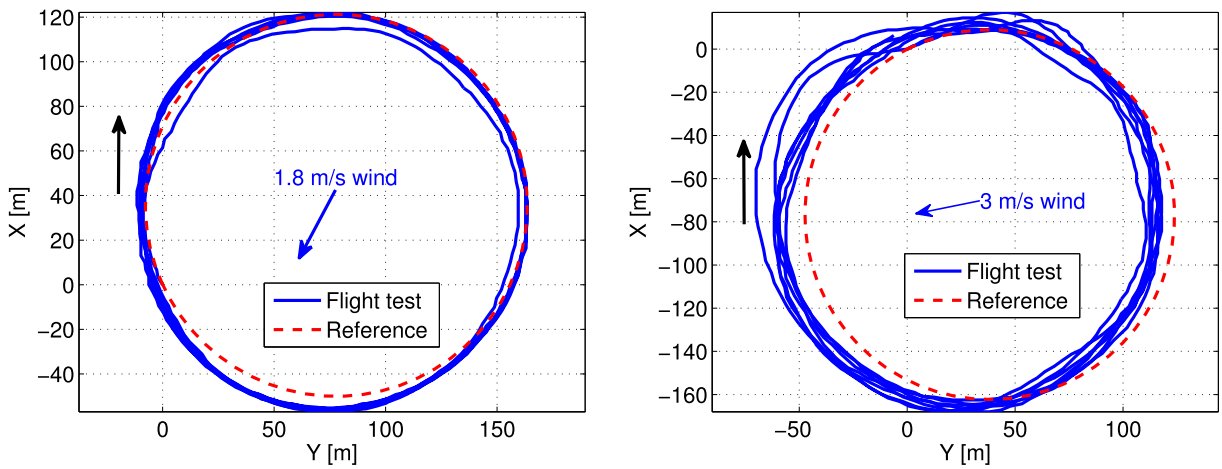

Fig. 28 Performance of an H_∞ controller in tracking a circular trajectory (black arrows indicate the flight direction; blue arrows indicate the wind direction)

controller based on the derived model and tested it on the platform. The performance of the controller in tracking the reference circular trajectory under two wind conditions (1.8 m/s and 3 m/s average wind speed) is demonstrated in Fig. 28. As the ultimate goal of developing this platform is the implementation of advanced control algorithms, these preliminary flight control tests are promising.

In conclusion, the complete flight dynamic model of the UAV includes the servomotor dynamics, where each servomotor is modeled as a second-order system as given in Eq. 7, in addition to the nonlinear equations of motion given in Eq. 5, with the relationships mapping the state and control variables to the aerodynamic forces and moments provided in Eq. 8 and the look-up tables mapping the throttle command and airspeed to the generated propeller thrust represented graphically in Figs. 16 and 17.

4 Conclusions

In this paper, the complete development process of a UAV platform for advanced control implementation is discussed. The airframe of the platform is obtained from an off-the-shelf R/C model airplane, the Telemaster, which is modified to incorporate onboard computers along with several standard and customized sensors. Two airdata probes are developed, tested, and calibrated to measure the angle of attack, sideslip, and airspeed of the UAV. Two computers are installed onboard the airplane with each assigned specific tasks. The resulting architecture enables the implementation of a control algorithm without interference from such basic functions as sensor data reading, servo actuation, and data communication.

A mathematical model of the airplane and other substantial subsystems is obtained using theoretical and empirical tools. Specifically, the output error method is employed to estimate the longitudinal and lateral-directional aerodynamic parameters of a postulated model from flight test data. A second-order model of the servomotors is derived from the frequency response. In addition, a propulsion model is generated using in part the Javaprop applet.

References

1. Ardupilot Mega. http://plane.ardupilot.com/. Accessed 23 July 2014 (2014)
2. USA Standard Atmosphere. USA Government Printing Office, Washington (1976)
3. Arifianto, O.: A low-cost unmanned aerial vehicle research platform: Development, modeling, and advanced control implementation. Ph.D. thesis, Department of Aerospace and Ocean Engineering, Virginia Tech (2013)
4. Arifianto, O., Farhood, M.: Optimal control of fixed-wing uavs along real-time trajectories. In: 5th Annual DSCC and 11th MOVIC (2012)
5. Barlow, J.B., Rae, W.H., Pope, A. Low-speed wind tunnel testing, 3rd edn. Wiley-Interscience (1999)
6. Bryer, D.W., Walshe, D.E.: Pressure probes selected for three-dimensional flow measurement. Reports and memoranda 3037, national advisory committee for aeronautics (1955)
7. Cabecinhas, D., Silvestre, C., Rosa, P., Cunha, R.: Path-following control for coordinated turn aircraft maneuvers. In: AIAA Guidance, Navigation and Control Conference and Exhibit (2007)
8. Craig, J.J. Introduction to robotics: mechanics and control, 2nd edn. Addison-Wesley Longman Publishing Co., Inc., MA, USA (1989)
9. Dansker, O.D., Johnson, M.J., Selig, M.S., Bretl, T.W.: Development of the uiuc aero testbed: a large-scale unmanned electric aerobatic aircraft for aerodynamics research. In: (AIAA) Applied Aerodynamics Conference (2013)
10. Dominy, R.G., Hodson, H.P.: An investigation of factors influencing the calibration of five-hole-probe for three-dimensional flow measurements. J. Turbomach. **115**, 513–519 (1993)
11. Dorobantu, A., Murch, A., Mettler, B., Balas, G.: System identification for small, low-cost, fixed-wing unmanned aircraft. J. Aircr. **50**(4), 1117–1130 (2013)
12. Farhood, M.: Nonstationary LPV control for trajectory tracking: a double pendulum example. Int. J. Control. **85**(5), 545–562 (2012)
13. Farhood, M., Di, Z., Dullerud, G.E.: Distributed control of linear time-varying systems interconnected over arbitrary graphs. International Journal of Robust and Nonlinear Control doi:10.1002/rnc.3081
14. Farhood, M., Dullerud, G.E.: Control of nonstationary LPV systems. Automatica **44**(8), 2108–2119 (2008)
15. Farhood, M., Dullerud, G.E.: Control of systems with uncertain initial conditions. IEEE Trans. Autom. Control **53**(11), 2646–2651 (2008)
16. Fisher, R.A.: On the mathematical foundations of theoretical statistics. Philosophical Transactions of the Royal Society of London. Series A, Containing Papers of a Mathematical or Physical Character 222, pp. 309368. http://www.jstor.org/stable/91208. Accessed 23 July 2014 (1922)
17. Gibbs, B.P.: Advanced Kalman filtering, least-squares and modeling: A practical handbook. Wiley, Hoboken, NJ (2011)

18. Gracey, W.: Summary of methods of measuring angle of attack. Technical note 4351, national advisory committee for aeronautics (1958)
19. Green, M.W.: Measurement of the moments of inertia of full scale airplanes. NACA technical note (1927)
20. Hartley, R.F., Hugon, F.: Development and flight testing of a model based autopilot library for a low cost unmanned aerial systems. In: (AIAA) Guidance, navigation and control conference (2013)
21. Hepperle, M.: Javaprop - design and analysis of propellers. http://www.mh-aerotools.de/airfoils/javaprop.htm
22. J. E. Zeis, C.U.: Angle of attack and sideslip estimation using inertial reference platform. Master's thesis, Air Force Institute of Technology (1988)
23. Jardin, M.R., Mueller, E.R.: Optimized measurements of unmanned-air-vehicle mass moment of inertia with a bifilar pendulum. J. Aircr. **46**, 63–75 (2009)
24. Jategaonkar, R.V.: Flight Vehicle System Identification: a time domain methodology. Progress in astronautics and aeronautics. American Institute of Aeronautics and Astronautics (2006)
25. Jordan, T., Foster, J., Bailey, R., Belcastro, C.: Airstar: a uav platform for flight dynamics and control system testing. In: (AIAA) 25th Aerodynamic and Measurement Technology and Ground Testing Conference (2006)
26. Jung, D., Levy, E.J., Zhou, D., Fink, R., Moshe, J., Earl, A., Tsiotras, P.: Design and development of a low-cost test-bed for undergraduate education in UAVs. In: Proceedings of the 44th IEEE Conference on Decision and Control, and the European Control Conference 2005, pp. 27392744. Seville, Spain (2005)
27. Kaminer, I., Pascoal, A., Hallberg, E., Silvestre, C.: Trajectory tracking for autonomous vehicles: An integrated approach to guidance and control. J. Guid. Control. Dyn. **21**(1), 29–38 (1998)
28. Kane, T.R., tai Tseng, G.: Dynamics of the bifilar pendulum. Int. J. Mech. Sci. **9**, 83–96 (1967)
29. Klein, V., Morelli, E.A.: Aircraft system identification: theory and practice. American Institute of Aeronautics and Astronautics (2006)
30. Manaï, M., Desbiens, A., Gagnon, E.: Identification of a UAV and design of a hardware-in-the-loop system for nonlinear control purposes. In: Proceedings of the AIAA Guidance, Navigation, and Control Conference (2005)
31. Drela, M.: AVL. http://web.mit.edu/drela/Public/web/avl/. Accessed 23 July 2014
32. McLain, T.W., Beard, R.W.: Unmanned air vehicle testbed for cooperative control experiments. In: Proceedings of the American Control Conference, vol. 6, pp. 53275331. Boston, MA (2004)
33. Miller, M.P.: An accurate method of measuring the moments of inertia of airplanes. NACA Technical Note (1930)
34. Morelli, E.: Real-time aerodynamic parameter estimation without air flow angle measurements. J. Aircr. **49**(4), 1064–1074 (2012)
35. Morrison, G.L., Schobeiri, M.T., Pappu, K.R.: Five-hole pressure probe analysis technique. Flow Meas. Instrum. **9**, 153–158 (1998)
36. Motter, M.A., Logan, M.J., French, M.L., Guerreiro, N.M.: Simulation to flight test for a UAV controls testbed. In: Proceedings of the 25th AIAA Aerodynamic Measurement Technology and Ground Testing Conference. San Francisco, CA (2006)
37. Mulder, J.A., Chu, Q.P., Sridhar, J.K., Breeman, J.H., Laban, M.: Non-linear aircraft flight path reconstruction review and new advances. Prog. Aerosp. Sci. **35**, 673–726 (1999)
38. Murch, A.M., Paw, Y.C., Pandita, R., Li, Z., Balas, G.J.: A low cost small UAV flight research facility. In: Holzapfel, F., Theil, S. (eds.): Advances in Aerospace Guidance, Navigation and Control, pp. 29–40. Springer, Berlin Heidelberg (2011)
39. Naughton, J.W., III, L.N.C., Settles, G.S.: A miniature, fast-response 5-hole probe for supersonic flowfield measurements. In: (AIAA) 30th Aerospace Sciences Meeting & Exhibit (1992)
40. Owens, D.B., Cox, D.E., Morelli, E.A.: Development of a low-cost sub-scale aircraft for flight research: the faser project. In: (AIAA) Aerodynamic Measurement Technology and Ground Testing Conference (2006)
41. Paul, A.R., Upadhyay, R.R., Jain, A.: A novel calibration algorithm for five-hole pressure probe. Int. J. Eng. Sci. Tech. **3**, 88–95 (2011)
42. Pereira, E., Hedrick, K., Sengupta, R.: The C3UV testbed for collaborative control and information acquisition using UAVs. In: Proceedings of the American Control Conference, pp. 14661471. Washington, DC (2013)
43. Raol, J., Singh, J.: Flight mechanics modeling snd analysis. CRC Press (2009)
44. Salman, S.A., Sreenatha, A.G., Choi, J.Y.: Attitude dynamics identification of unmanned aerial vehicle. Int J Control. Autom. Syst. **4**(6), 782–787 (2006)
45. Soule, H.A., Miller, M.P.: Experimental determination of the moments of inertia of airplanes. NACA Technical Report (1933)
46. Telionis, D., Yang, Y., Rediniotis, O.: Recent development in multi-hole probe (mhp) technology. In: 20th International Congress of Mechanical Engineering (2009)
47. Tischler, M.B., Remple, R.K.: Aircraft and rotorcraft system identification: engineering methods with flight test examples. Am. Inst. Aeronaut. Astronaut. (2006)
48. Tomas, M.: Tornado, http://www.redhammer.se/tornado/index.html. Accessed 23 July 2014
49. V.Hoffer, N., Coopmans, C., Jensen, A.M., Chen, Y.: A survey and categorization of small low-cost unmanned aerial vehicle system identification. J. Intell. & Robot. Syst. **74**(1–2), 129–145 (2014)
50. Walther, B.A., Moore, J.L.: The concepts of bias, precision and accuracy, and their use in testing the performance of species richness estimators, with a literature review of estimator performance. Ecography **28**(6), 815–829 (2005)
51. Williams, J.E., Vukelich, S.R.: The USAF stability and control digital DATCOM volume 1 users manual. DTIC-MIL (1979)